UNITED NATIONS EDUCATIONAL, SCIENTIFIC AND CULTURAL ORGANIZATION
INTERNATIONAL ATOMIC ENERGY AGENCY
INTERNATIONAL CENTRE FOR THEORETICAL PHYSICS
I.C.T.P., P.O. BOX 586, 34100 TRIESTE, ITALY, CABLE: CENTRATOM TRIESTE

H4.SMR/984-2

Winter College on Quantum Optics: Novel Radiation Sources

3-21 March 1997

Quantum optics of single atoms

H. Walther

Max-Planck-Institute for Quantum Optics, Garching bei München, Germany

The Quantum Optics of Single Atoms

H. Walther

Sektion Physik der Universität München and
Max-Planck-Institut für Quantenoptik
85748 Garching, Fed. Rep. of Germany

Abstract:

In recent years quite a few experiments on the interaction of radiation with single atoms in cavities and traps have been performed emphasising the quantum features of the interaction. A brief review of recent experiments of this type will be given. Since traps allow to probe the same atom for a long time and, in addition, to study the detailed time behaviour of the radiation-atom interaction e.g. by observing quantum jumps, it is promising to combine optical cavities with high quality factors with the known trapping techniques. It is shown that a single atom laser with interesting new features can be realised.

The following papers give an introduction to the lectures which will be presented at the Winter College on Quantum Optics. They consist of the following reviews:

1. Atomic Interferometry with the Micromaser
2. The Ion Trap Laser
3. Spectroscopy with Trapped Ions
4. Resonance Fluorescence of a Single Ion.

Atomic interferometry with the micromaser

by *Herbert Walther*

Max-Planck-Institut für Quantenoptik,
85748 Garching, Germany and
Sektion Physik, Ludwig-Maximilians-Universität München,
80333 München, Germany

Abstract. In this paper recent experiments with the one-atom maser or micromaser are described. They deal with the dynamical behavior of the field at parameter values where the field undergoes phase transitions. Furthermore atomic interferences are observed in the micromaser when the inversion of the atoms leaving the cavity is measured while the cavity frequency is scanned across the atomic resonance. The interferences are due to the nonadiabatic mixing of dressed states at the entrance and exit holes of the maser cavity. The interference structures are triangular shaped and approximately equidistant. They are associated with the dynamics of the atom-field interaction, show quantum jumps, and demonstrate bistability of the micromaser field.

The one-atom maser or micromaser allows one to study the resonant interaction of a single atom with a single mode of a superconducting niobium cavity (Meschede, Walther and Müller, 1985; Rempe, Walther and Klein, 1987; Rempe, Schmidt-Kaler and Walther, 1990; Rempe and Walther, 1990). In previous experiments values of the quality factor as high as 3×10^{10} have been achieved for the resonant mode, corresponding to an average lifetime of a photon in the cavity of 0.2 s. The photon lifetime is thus much longer than the interaction time of an atom with the maser field. The atoms used in the experiments are rubidium Rydberg atoms pumped by laser excitation into the upper level of the maser transition, which is usually induced between neighboring Rydberg states. In the experiments the atom-field interaction is probed by observing the population in the upper and lower maser levels after the atoms have left the cavity. The field in the cavity consists only of single or a few photons. Nevertheless, it is possible to study the interaction in considerable detail. The dynamics of the atom-field interaction treated with the Jaynes-Cummings model was investigated by selecting and varying the velocity of the pump atoms (Rempe, Walther and Klein, 1987). The counting statistics of the pump atoms emerging from the cavity allowed us to measure the non-classical

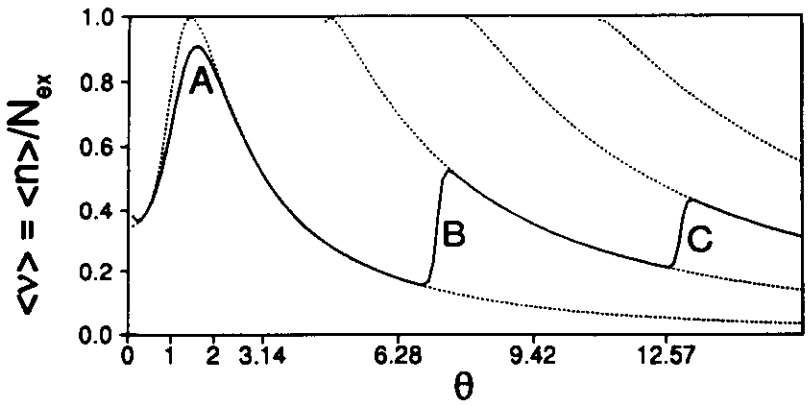

Figure 1. Mean value of $\nu = n/N_{ex}$ versus the pump parameter $\Theta = \Omega t_{int}\sqrt{N_{ex}}/2$, where the value of Θ is changed via N_{ex}. The solid line represents the micromaser solution for $\Omega = 36kHz, t_{int} = 35\mu s$, and temperature $T = 0.15K$. The dotted lines are semiclassical steady-state solutions corresponding to fixed stable gain=loss equilibrium photon numbers (Meystre, 1992). The crossing points between a line Θ = const and the dotted lines correspond to the values where minima in the Fokker-Planck potential $V(\nu)$ occur.

character of the cavity field (Rempe, Schmidt-Kaler, Walther, 1990; Rempe, Walther, 1990) predicted by the micromaser theory. It also has been observed that under suitable experimental conditions the maser field exhibits metastability and hysteresis (Benson, Raithel, Walther, 1994). Most of the maser experiments so far have been performed at cavity temperatures of 0.5 K. Recently, a further reduction of the temperature to below 0.1 K was achieved by using an improved setup in a dilution refrigerator (Benson, Raithel, Walther, 1994).

In the following we are going to review two recent experiments which deal with the observation of quantum jumps of the micromaser field and with the observation of atomic interferometry in the cavity (Raithel, Benson, Walther, 1995). For a review of the previous work see Raithel et al. (1994).

Under steady-state conditions, the photon statistics P(n) of the field is essentially determined by the pump parameter, $\Theta = N_{ex}^{1/2}\Omega t_{int}/2$ (Filipowicz, Javanainen, Meystre, 1986; Lugiato, Scully, Walther, 1987; Raithel et al., 1994). Here, N_{ex} is the average number of atoms that enter the cavity during τ_{cav}, Ω the vacuum Rabi flopping frequency, and t_{int} is the atom-cavity interaction time. The quantity $\langle\nu\rangle = \langle n\rangle/N_{ex}$ shows the following generic behavior (see Fig. 1): It suddenly increases at the maser threshold value $\Theta = 1$, and reaches a maximum for $\Theta \approx 2$ (denoted

by A in Fig. 1). The maser threshold shows the characteristics of a continuous phase transition (Filipowicz, Javanainen, Meystre, 1986; Lugiato, Scully, Walther, 1987). As Θ further increases, $\langle\nu\rangle$ decreases and reaches a minimum at $\Theta \approx 2\pi$, and then abruptly increases to a second maximum (B in Fig. 1). This general type of behavior recurs roughly at integer multiples of 2π, but becomes less pronounced with increasing Θ. The reason for the periodic maxima of $\langle\nu\rangle$ is that for integer multiples of $\Theta = 2\pi$ the pump atoms perform an almost integer number of full Rabi flopping cycles, and start to flip over at a slightly larger value of Θ, thus leading to enhanced photon emission. The periodic maxima in $\langle\nu\rangle$ for $\Theta = 2\pi, 4\pi, \ldots$ can be interpreted as first-order phase transitions (Filipowicz, Javanainen, Meystre, 1986; Lugiato, Scully, Walther, 1987). The field strongly fluctuates for all phase transitions (A, B, and C in Fig. 1), the large photon number fluctuations for $\Theta \approx 2\pi$ and multiples thereof being caused by the presence of two maxima in the photon number distribution P(n) at photon numbers n_l and n_h ($n_l < n_h$). For n_l and n_h the atoms perform almost integer numbers m or m + 1 of full Rabi flopping cycles, respectively. If the pump parameter is scanned across $\Theta \approx 2\pi m$, the maximum of P(n) at n_l completely dies out, and is replaced by the new peak at the higher photon number n_h. For $\Theta \approx 2\pi m$, the simultaneous presence of two maxima of P(n) leads to spontaneous jumps of the micromaser field between two average photon numbers n_l and n_h.

The phenomenon of the two coexisting maxima in P(n) was also studied in a semi-heuristic Fokker-Planck (FP) approach (Filipowicz, Javanainen, Meystre, 1986; Lugiato, Scully, Walther, 1987). There, the photon number distribution P(n) is replaced by a probability function $P(\nu, \tau)$ with continuous variables $\tau = t/\tau_{cav}$ and $\nu(n) = n/N_{ex}$, the latter replacing the photon number n. The steady-state solution obtained for $P(\nu, \tau), \tau \gg 1$, can be constructed by means of an effective potential $V(\nu)$ showing minima at positions where maxima of $P(\nu, \tau), \tau \gg 1$, are found. Close to $\Theta = 2\pi$ and multiples thereof, the effective potential $V(\nu)$ exhibits two equally attractive minima located at stable gain-loss equilibrium points of maser operation (Meystre, 1992) (see Fig. 1). The mechanism at the phase transitions mentioned is always the same: A minimum of $V(\nu)$ loses its global character when Θ is increased, and is replaced in this role by the next one. This reasoning is a variation of the Landau theory of first-order phase transitions, with $\sqrt{\nu}$ being the order parameter. This analogy actually leads to the notion that in the limit $N_{ex} \to \infty$ the change of the micromaser field around integer multiples $\Theta = 2\pi$ can be interpreted as first-order phase transitions.

Close to first-order phase transitions long field evolution time constants τ_{field} are expected (Filipowicz, Javanainen, Meystre, 1986; Lugiato, Scully, Walther, 1987). This phenomenon is experimentally demonstrated in this paper, as well as related phenomena, such as spontaneous quantum jumps between equally attractive minima of $V(\nu)$, bistability, and hysteresis. Some of those phenomena are also predicted in the two-photon micromaser (Raithel, Benson, Walther, 1995), for which quali-

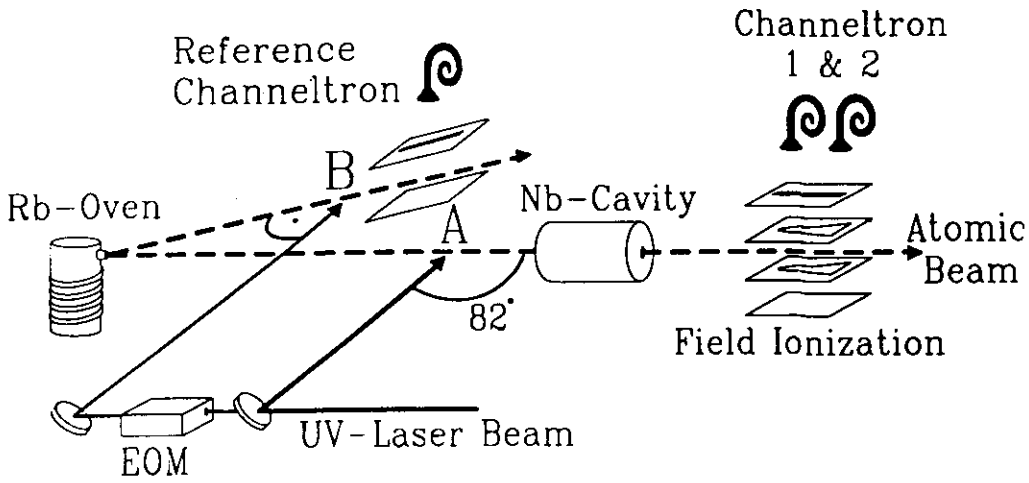

Figure 2. Sketch of the experimental setup. The rubidium atoms emerge from an atomic beam oven and are excited at an angle of 82° at location A. After interaction with the cavity field, they enter a state-selective field ionization region, where channeltrons 1 and 2 detect atoms in the upper and lower maser levels, respectively. A small fraction of the UV radiation passes through an electro-optic modulator (EOM), which generates sidebands of the UV radiation. The blueshifted sideband is used to stabilize the frequency of the laser onto the Doppler-free resonance monitored with a secondary atomic beam produced by the same oven (location B).

tative evidence of first-order phase transitions and hysteresis is reported (Raimond et al., 1989).

The experimental setup used is shown in Fig. 2. It is similar to that described by Rempe and Walther (1990) and Benson, Raithel and Walther (1994). As before, ^{85}Rb atoms were used to pump the maser. They are excited from the $5S_{1/2}, F = 3$ ground state to $63P_{3/2}, m_J = \pm 1/2$ states by linearly polarized light of a frequency-doubled c.w. ring dye laser. The polarization of the laser light is linear and parallel to the likewise linearly polarized maser field, and therefore only $\Delta m_J = 0$ transitions are excited. Superconducting niobium cavities resonant with the transition to the $61D_{3/2}, m_J = \pm 1/2$ states were used; the corresponding resonance frequency is 21.506 GHz. The experiments were performed in a $^3He/^4He$ dilution refrigerator with cavity temperatures $T \approx 0.15K$. The cavity Q values ranged from 4×10^9 to 8×10^9. The velocity of the Rydberg atoms and thus their interaction time t_{int} with the cavity field were preselected by exciting a particular velocity subgroup with the laser. For this purpose, the laser beam irradiated the atomic beam at an angle of approximately 82°. As a consequence, the UV laser light (linewidth $\approx$

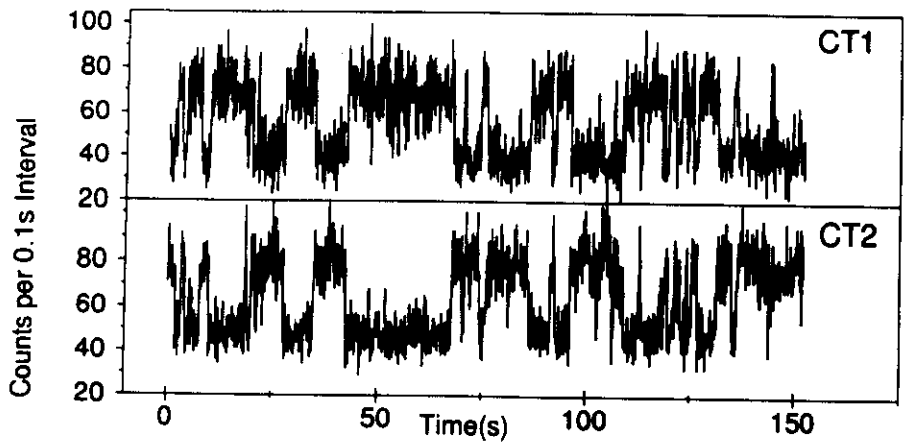

Figure 3. Quantum jumps between two equally stable operation points of the maser field. The channeltron counts are plotted versus time (CT1 = upper state and CT2 = lower state signals).

2 MHz) is blueshifted by 50-200 MHz by the Doppler effect, depending on the velocity of the atoms.

Information on the maser field and interaction of the atoms in the cavity can be obtained solely by state-selective field ionization of the atoms in the upper or lower maser level after they have passed through the cavity. The field ionization detector was recently modified, so that there is now a detection efficiency of $\eta = (35 \pm 5)\%$. For different t_{int} the atomic inversion has been measured as a function of the pump rate by comparing the results with micromaser theory (Filipowicz, Javanainen, Meystre, 1986; Lugiato, Scully, Walther, 1987), the coupling constant Ω is found to be $\Omega = (40 \pm 10)$krad/s.

Depending on the parameter range, essentially three regimes of the field evolution time constant τ_{field} can be distinguished. Here we only discuss the results for intermediate time constants. The maser was operated under steady-state conditions close to the second first-order phase transition (C in Fig. 1). The interaction time was $t_{int} = 47\mu s$ and the cavity decay time $\tau_{cav} = 60ms$. The value of N_{ex} necessary to reach the second first-order phase transition was $N_{ex} \approx 200$. For these parameters, the two maxima in P(n) are manifested in spontaneous jumps of the maser field between the two maxima with a time constant of $\approx 5s$. This fact and the relatively large pump rate led to the clearly observable field jumps shown in Fig. 3. Because of the large cavity field decay time, the average number of atoms

in the cavity was still as low as 0.17. The two discrete values for the counting rates correspond to the metastable operating points of the maser, which correspond to ≈ 70 and ≈ 140 photons. In the FP description, the two values correspond to two equally attractive minima in the FP potential $V(\nu)$. If one considers, for instance, the counting rate of lower-state atoms (CT2 in Fig. 3), the lower (higher) plateaus correspond to time intervals in the low (high) field metastable operating point. If the actual photon number distribution is averaged over a time interval containing many spontaneous field jumps, the steady-state result P(n) of the micromaser theory is recovered.

In the parameter ranges where switching occurs much faster than in the case shown in Fig. 3 the individual jumps cannot be resolved, therefore different methods have to be used for the measurement. Furthermore hysteresis is observed at the maser parameters for which the field jumps occur. Owing to lack of space these results cannot be discussed here. For a complete survey on the performed experiments it is referred to Benson, Raithel, and Walther (1994).

In the following we would like to discuss the recent experiment on atomic interferometry in the micromaser (Raithel, Benson, Walther, 1995). Since a non-classical field is generated in the maser cavity, we were able for the first time to investigate atomic interference phenomena under the influence of non-classical radiation; owing to the bistable behavior of the maser field the interferences display quantum jumps, thus the quantum nature of the field gets directly visible in the interference fringes. Interferences occur since a coherent superposition of dressed states is produced by mixing the states at the entrance and exit holes of the cavity. Inside the cavity the dressed states develop differently in time, giving rise to Ramsey-type interferences (Ramsey, 1956) when the maser cavity is tuned through resonance.

The setup used in the experiment is identical to the one described before (Benson, Raithel, Walther, 1994). However, the flux of atoms through the cavity is by a factor of 5 - 10 higher than in the previous experiments, where the $63P_{3/2}-61D_{5/2}$ transition was used. For the experiments the Q-value of the cavity was 6×10^9 corresponding to a photon decay time of 42 ms.

Fig. 4 shows the standard maser resonance in the uppermost plot which is obtained when the resonator frequency is tuned. At large values of $N_{ex}(N_{ex} > 89)$ sharp, periodic structures appear. These typically consist of a smooth wing on the low- frequency side, and a vertical step on the high-frequency side. The clarity of the pattern rapidly decreases when N_{ex} increases to 190 or beyond. We will see later that these structures have to be interpreted as interferences. It can be seen that the atom-field resonance frequency is red-shifted with increasing N_{ex}, the shift reaching 200 kHz for $N_{ex} = 190$. Under these conditions there are roughly 100

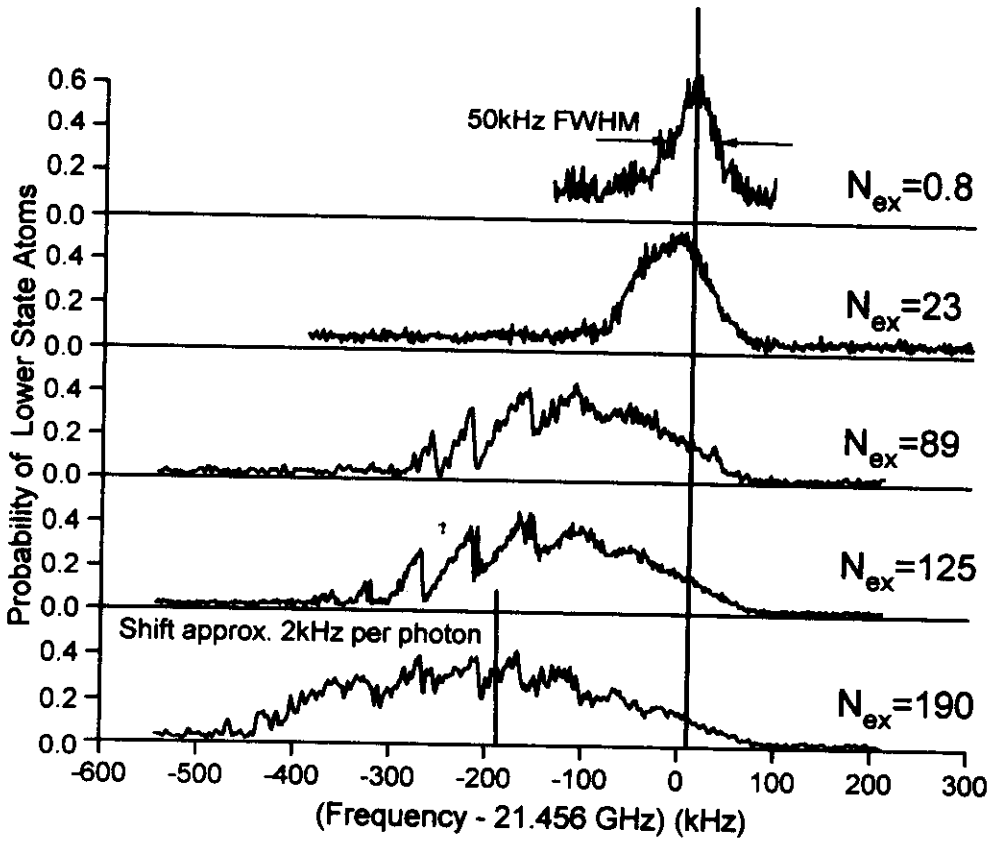

Figure 4. Shift of the maser resonance $63P_{3/2} - 61D_{5/2}$ for fast atoms ($t_{int} = 35\mu s$). The upper plot shows the maser line for low pump rate ($N_{ex} < 1$).The FWHM linewidth (50 kHz) sets an upper limit of $\approx 5mV/cm$ for the residual electric stray fields in the center of the cavity. The lower resonance lines are taken for the indicated large values of N_{ex}.The plots show that the center of the maser line shifts by about 2 kHz per photon. In addition, there is considerable field-induced line broadening which is approximately proportional to $\sqrt{N_{ex}}$. For $N_{ex} \geq 89$ the lines display periodic structures, which are discussed in the text.

photons on the average in the cavity. The large red-shift cannot be explained by AC Stark effect, which for 100 photons would amount to about one kHz for the transition used. Therefore it is obvious that other reasons must be responsible for the observed shift.

It is known from previous maser experiments that there are small static electric fields in the entrance and exit holes of the cavity. It is supposed that this field

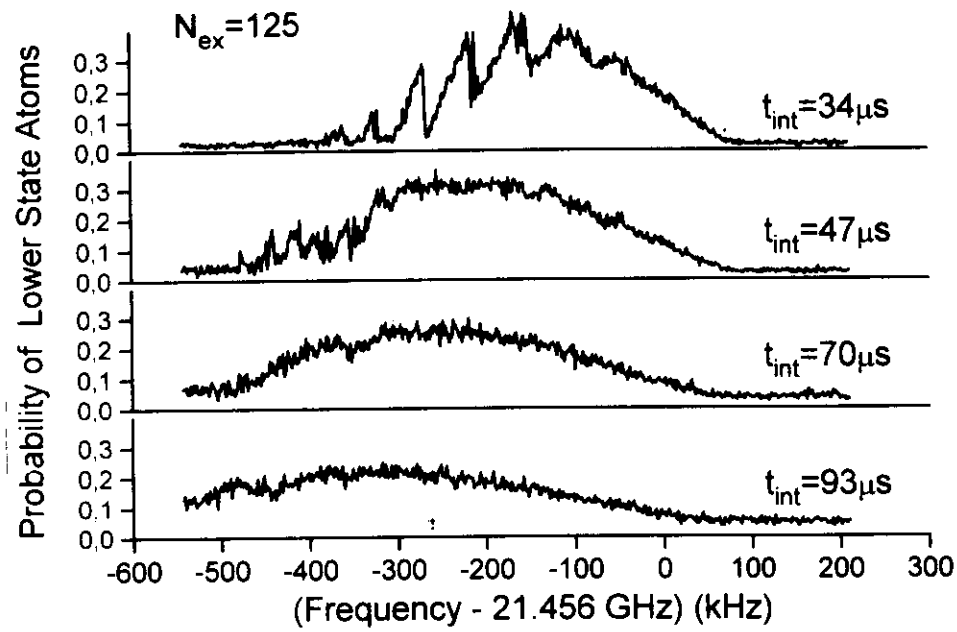

Figure 5. Maser resonance lines for large N_{ex} and the indicated values of t_{int}. The period and visibility of the additional structures reduce when t_{int} is increased. Furthermore the center of the resonance shifts to lower frequency with increasing t_{int}.

is generated by patch effects at the surface of the niobium metal caused by rubidium deposits caused by the atomic beam or by microcrystallites formed when the cavities are tempered after machining. The tempering process is necessary to achieve high quality factors. The influence of those stray fields is only observable in the cavity holes; in the center of the cavity they are negligible owing to the large atom-wall distances.

Fig. 5 shows the variation of the structure when the interaction time t_{int} between the atoms and the cavity field is changed. The uppermost recording is the same as the second from below in Fig. 4. For large t_{int} no clear substructures can be observed. In the second plot from the top a substructure is still present on the left side, but it is less pronounced than in the uppermost one. The upper two plots in Fig. 5 show that the period of the substructures reduces with increasing interaction time. The substructure disappears for $t_{int} > 47\mu s$. Furthermore, an increasing shift of the whole structure to low frequencies is observed when t_{int} is increased.

In order to understand the observed structures, we first have to analyze the Jaynes-Cummings dynamics of the atoms in the cavity. This treatment is more involved than that in connection with previous experiments, since the higher maser field requires detailed consideration of the field in the periphery of the cavity, where the additional influence of stray electric fields is more important.

The usual formalism for the description of the coupling of an atom to the radiation field is the dressed atom approach (Cohen-Tannoudji, Dupont-Roc, Grynberg, 1992), leading to splitting of the coupled atom-field states, depending on the vacuum Rabi-flopping frequency Ω, the photon number n, and the atom-field detuning δ. We face a special situation at the entrance and exit holes of the cavity. There we have a position-dependent variation of the cavity field, as a consequence of which Ω is position-dependent. An additional variation results from the stray electric fields in the entrance and exit holes. Owing to the Stark-effect these fields lead to a position-dependent atom-field detuning δ.

The Jaynes-Cummings-Hamiltonian only couples pairs of dressed states. Therefore, it is sufficient to consider the dynamics within such a pair. In our case, prior to the atom-field interaction the system is in one of the two dressed states. For parameters corresponding to the periodic substructures in Figs. 4 and 5 the dressed states are mixed only at the beginning of the atom-field interaction and at the end. The mixing at the beginning creates a coherent superposition of the dressed states. Afterwards the system develops adiabatically, whereby the two dressed states accumulate a differential dynamic phase Φ which strongly depends on the cavity frequency. The mixing of the dressed states at the entrance and exit holes of the cavity, in combination with the intermediate adiabatic evolution, generates a situation similar to a Ramsey two-field interaction.

The maximum differential dynamic phase Φ solely resulting from dressed-state coupling by the maser field is roughly 4Φ under the experimental conditions used here. This is not sufficient to explain the interference pattern of Fig. 4, where we have at least six maxima corresponding to a differential phase of 12 π. This means that an additional energy shift differently affecting upper and lower maser states is present. Such a phenomenon can be caused by the above mentioned small static electric fields present in the holes of the cavity. The static field causes a position-dependent detuning δ of the atomic transition from the cavity resonance; as a consequence we get an additional differential dynamic phase Φ. In order to interpret the periodic substructures as a result of the variation of Φ with the cavity frequency, the phase Φ has to be calculated from the atomic dynamics in the maser field.

The quantitative calculation can be performed on the basis of the micromaser theory. A theoretical result of $\langle n \rangle / N_{ex}$ obtained in this way is shown in Fig. 6. The uppermost plot shows the maser resonance line expected without any static

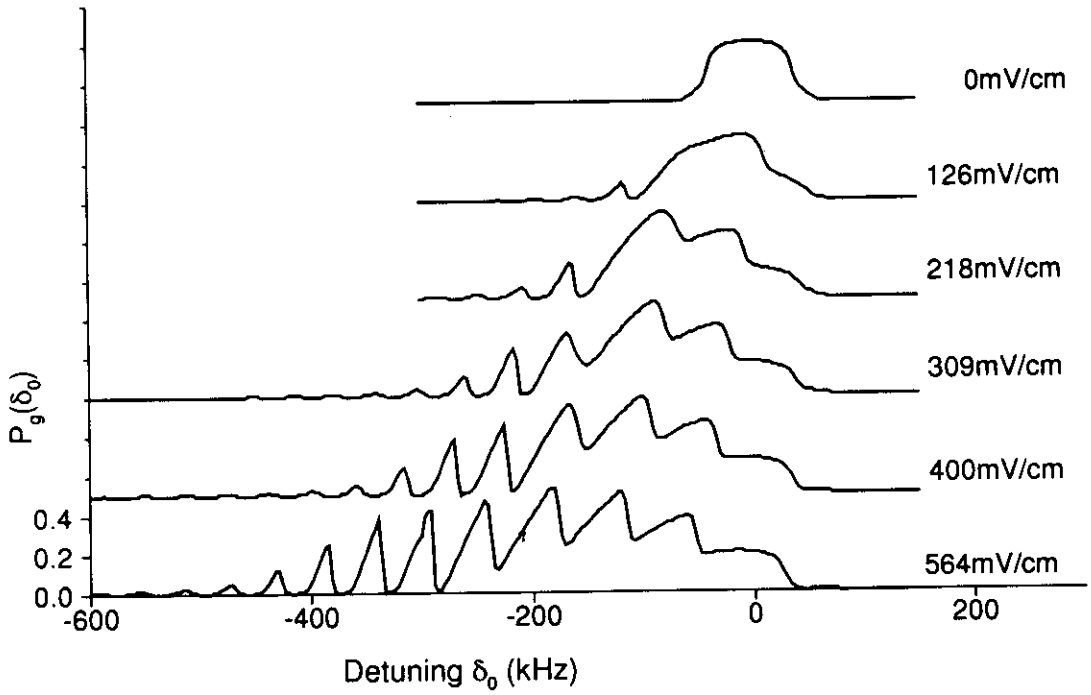

Figure 6. Theoretical maser lines for the indicated values of the static electric field strength in the cavity holes. The theoretical model is explained in the text. In the calculation we use $N_{ex} = 100$ and $\Omega = 45krad/s$. The interaction time is $t_{int} = 35\mu s$, and the RMS deviation of the interaction time is 1 μs. In order to account for the fluctuations of the dynamic phases induced by the inhomogeneity of the stray electric fields, a Gaussian distribution of the atom-field detuning with a RMS deviation of 5 kHz is assumed (see also Benson, Raithel and Walther, 1994).

electric field. With increasing DC field strength in the cavity holes the structure changes, the curve for 309 mV/cm coming very close to those displayed in Fig. 4 for $N_{ex} = 89$ and 125, and at the top of Fig. 5. We have to stress that the field values indicated in Fig. 6 correspond to the maximum field strength in the cavity holes. The field value in the central part of the cavity is roughly 100 times smaller, and therefore without significance in low-flux maser experiments. Fig. 6 also shows that the qualitative structure of the maser line is the same for all fields larger than about 200 mV/cm.

The calculations also reproduce the experimental finding that the maser line shifts to lower frequencies when N_{ex} is increased. The mechanism for that can be explained as follows: the high-frequency edge of the maser line does not shift with N_{ex}

at all, since this part of the resonance is produced in the central region of the cavity, where practically no static electric fields are present. The low-frequency cutoff of the structure is determined by the location where the mixing of the dressed states occurs. With decreasing cavity frequency those points shift closer to the entrance and exit holes, with the difference between the particular cavity frequency and the unperturbed atomic resonance frequency giving a measure of the static electric field at the mixing locations. Closer to the holes the passage behavior of the atoms through the mixing locations gets non-adiabatic for the following reasons: firstly, the maser field strength reduces towards the holes. This leads to reduced repulsion of the dressed states. Secondly, the stray electric field strongly increases towards the holes. This implies a larger differential slope of the dressed state energies at the mixing locations, and therefore leads to a stronger non-adiabatic passage. At the same time the observed signal extends further to the low frequency spectral region. Since the photon emission probabilities are decreasing towards lower frequencies their behavior finally defines the low-frequency boundary of the maser resonance line. With increasing N_{ex} the photon number n increases. As for larger values of n the photon emission probabilities get larger, also an increasing N_{ex} leads to an extension of the range of the signal to lower frequencies. This theoretical expectation is in agreement with the experimental observation.

In the experiment it is also found that the maser line shifts towards lower frequencies with increasing t_{int} (Fig. 5). This result also follows from the developed model: the red-shift increases with t_{int} since a longer interaction time leads to a more adiabatic behavior in the same way as a larger N_{ex} does.

The calculations reveal that on the vertical steps displayed in the signal the photon number distribution has two distinctly separate maxima similar to those observed at the phase transition points discussed above. Therefore, the maser field should exhibit hysteresis and metastability under the present conditions as well. The hysteresis indeed shows up when the cavity frequency is linearly scanned up and down with a modest scan rate (Raithel et al., 1994). When the maser is operated in steady-state and the cavity frequency is fixed to the steep side of one of the fringes we also observe spontaneous jumps of the maser field between two metastable field states.

The calculations also show that on the smooth wings of the more pronounced interference fringes the photon number distribution P(n) of the maser field is strongly sub-Poissonian. This leads us to the conclusion that we observe Ramsey-type interferences induced by a non-classical radiation field. The sub-Poissonian character of P(n) results from the fact that on the smooth wings of the fringes the photon gain reduces when the photon number is increased. This feedback mechanism stabilizes the photon number resulting in a sub-Poissonian photon distribution.

The presented maser model explains all the observed experimental facts. The

periodic structures in the maser lines are thus interpreted as Ramsey-type interferences. If there was more accurate information on the DC fields in the cavity, a multilevel calculation taking into account the magnetic substructure of the involved fine-structure levels would make sense. Under the present conditions, however, the stray electric field amplitudes close to the cavity holes can only be estimated. The interference structure extends towards lower frequency as far as $\approx$ 500 kHz for $N_{ex} \approx 200$, this corresponding to an electric field of $\approx$ 25 mV/cm in a distance of roughly a few mm from the cavity holes.

To our knowledge it is the first time that it is demonstrated that non-adiabatic mixing can lead to Ramsey interferences. Besides other phenomena the bistable character of the micromaser field can be observed in jumps of the fringes; the observed interferences thus show a discontinuous behavior owing to the quantum properties of the field - it is the first time that such a discrete quantum behavior is directly observed in interference fringes. One of the applications of the described Ramsey interferometer could be the quantum-non-demolition measurement of the photon number in a cavity along the lines proposed by Brune et al. (1990). For this purpose the atoms in the cavity have to be dispersively coupled to a third level via a second quantum field which could agree with the frequency of another cavity mode.

References

Benson, O., Raithel, G., and Walther, H., (1994), Quantum jumps of the micromaser field - dynamic behavior close to phase transition points, *Phys. Rev. Lett.*, 72:3506.

Brune, M., Haroche, S., Lefevre, V., Raimond, J.M., and Zagury, N. (1990), Quantum nondemolition measurement of small photon numbers by Rydberg-atom phase-sensitive detection, *Phys. Rev. Lett.*, 65:976.

Cohen-Tannoudji, C., Dupont-Roc, J., Grynberg, G., (1992), *Atom-Photon Interactions* (John Wiley and Sons, Inc., N.Y.), pp. 407-514.

Filipowicz, P., Javanainen, J., and Meystre, P., (1986), Theory of a microscopic maser, *Phys. Rev. A*, 34:3077

Lugiato, L.A., Scully, M.O., and Walther, H., (1987), Connection between microscopic and macroscopic maser theory, *Phys. Rev. A*, 36:740.

Meschede, D., Walther, H., and Müller, G., (1985), The one-atom maser, *Phys. Rev. Lett.*, 54:551.

Meystre, P., (1992), Cavity quantum optics and the quantum measurement process, *Progress in Optics*, ed. E. Wolf (Elsevier Science Publishers, New York), 30:261.

Raimond, J.M., Brune, M., Davidovich, L., Goy, P., and Haroche, S., (1989), The two-photon Rydberg atom micromaser, *Atomic Physics*, eds. S. Haroche, J.C. Gay and G. Grynberg (World Scientific, Amsterdam), 11:441.

Raithel, G., Wagner, C., Walther, H., Narducci L.M., and Scully, M.O., (1994), The micromaser: a proving ground for quantum physics, *Advances in Atomic, Molecular, and Optical Physics, Supplement 2*, P. Berman (ed.), (Academic Press, New York), p. 57.

Raithel, G., Benson, O., and Walther, H., (1995), Atomic interferometry with the micromaser, *Phys. Rev. Lett.*, 75:3446.

Ramsey, N.F., (1956), *Molecular Beams* (Clarendon Press, Oxford), pp. 124-134.

Rempe, G., Walther H., and Klein, N., (1987), Observation of quantum collapse and revival in the one-atom maser, *Phys. Rev. Lett.*, 58:353.

Rempe, G., Schmidt-Kaler, F., and Walther, H., (1990), Observation of sub-Poissonian photon statistics in a micromaser, *Phys. Rev. Lett.*, 64:2783.

Rempe, G. and Walther, H., (1990), Sub-Poissonian atomic statistics in a micromaser, *Phys. Rev. A*, 42:1650.

EUROPHYSICS LETTERS 10 February 1997

Europhys. Lett., **37** (5), pp. 317-322 (1997)

Ion-trap laser

G. M. MEYER[1,3], H.-J. BRIEGEL[2] and H. WALTHER[1,3]

[1] *Max-Planck-Institut für Quantenoptik*
Hans-Kopfermann-Str. 1, D-85748 Garching, Germany
[2] *Lyman Laboratory of Physics, Harvard University*
ITAMP, Harvard-Smithsonian Center for Astrophysics
Cambridge, MA 02138, USA
[3] *Sektion Physik, Ludwig-Maximilians-Universität - München, Germany*

(received 9 September 1996; accepted in final form 10 January 1997)

PACS. 32.80–t – Photon interactions with atoms.
PACS. 42.50–p – Quantum optics.
PACS. 42.55–f – Lasers.

Abstract. – Laser operation with a single trapped Ca^+ ion in a high-finesse optical cavity is predicted at a wavelength of 866 nm. Different from a conventional laser, the formation of two thresholds can be observed. For both small and large pump strengths the field is quasi-thermal, in an intermediate region laser light with Poissonian and even sub-Poissonian statistics is produced. Atomic coherence effects play an important role. The multi-level system is treated by generalizing the pump-operator approach (*Europhys. Lett.*, **33** (1996) 515).

Advances in trapping and cooling of ions and atoms [1] as well as progress in cavity quantum electrodynamics with strong atom-field coupling in the optical regime [2] make an experimental realization of an ion-trap laser possible. Such a laser, schematically depicted in fig. 1*a*), will operate with a single ion as the active medium. Different from micromasers [3] and microlasers [4], this single ion will be kept in the cavity and stay in permanent interaction with the laser field. The resulting dynamics is very different from the situation when fresh atoms are injected into the cavity in a well-prepared state and as part of an atomic beam.

There have been several theoretical papers on one-atom lasers in the past [5]-[8]. This system provides a testing ground for new theoretical concepts and results in the quantum theory of the laser. Examples are atomic coherence effects [9] and dynamic (*i.e.* self-generated) quantum-noise reduction [10], [11], [8]. All these aspects are a consequence of a pump process whose complex nature is not accounted for in the standard treatment of the laser.

A formidable challenge for an experiment is the fact that a single atom or ion is responsible for maintaining the laser field. Mirrors with an ultra-high finesse are required, and a strong atom-field coupling is needed. After the emission of a photon, the ion has to be pumped before the next stimulated emission can occur. Similar as in the resonance fluorescence experiments which show antibunching [12], there is a certain time gap during which the ion is unable to add another photon to the laser field. It has been shown [8] that this time gap plays a significant role in the production of a field with sub-Poissonian photon statistics.

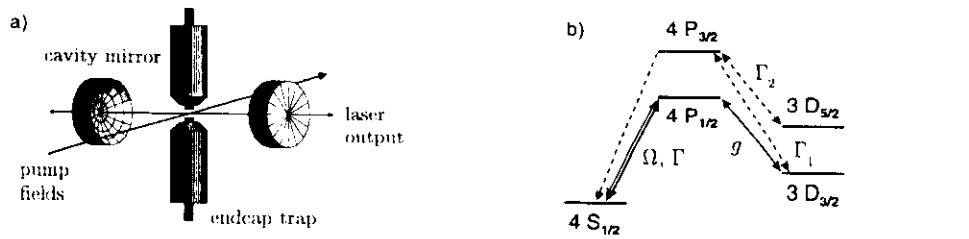

Fig. 1. – Schematic representation of *a*) an ion-trap laser and *b*) energy levels and transitions in Ca^+.

In this letter, we provide the theoretical basis for an experimental realization of the ion-trap laser. Our analysis takes into account details such as the multi-level structure, the coupling strengths and the parameters of the resonator. It has been a problem to find an ion with an appropriate level scheme. We find that it is possible to produce a laser field with the parameters of a single Ca^+ ion. This one-atom laser displays several features, which are not found in conventional lasers: the development of two thresholds, sub-Poissonian statistics, lasing without inversion and self-quenching.

We start with the treatment of a general multi-level scheme, such as the one depicted in fig. 1*b*). The ion interacts with a resonator mode and several pump fields, which will be realized by strong lasers and can be described classically. The number of photons in the quantized cavity mode, on the other hand, will be on the order of 10, corresponding to a flux of about 10^7 photons leaving the cavity per second.

The theoretical description is given in terms of a master equation

$$\frac{\partial}{\partial t}\mathrm{P} = \frac{1}{i\hbar}[H, \mathrm{P}] + L_{\mathrm{atom}}\mathrm{P} + L_{\mathrm{cav}}\mathrm{P}, \tag{1}$$

for the density operator P of the composed atom-and-cavity-mode system. The Hamiltonian H describes the interactions of the atom with the quantized laser mode and possible coherent pump fields, L_{atom} summarizes atomic relaxation processes as well as incoherent (broadband) pumping. Finally, $L_{\mathrm{cav}}\mathrm{P} = -(A/2)(a^\dagger a\mathrm{P} + \mathrm{P}a^\dagger a - 2a\mathrm{P}a^\dagger)$ describes the losses of the cavity, with the damping rate A for the mean photon number $\langle a^\dagger a\rangle$. The total state of the system can be expanded in terms of the bare atomic states, $\mathrm{P} = \sum_{\mathrm{LL}'} \rho_{\mathrm{LL}'}|\mathrm{L}\rangle\langle\mathrm{L}'|$, where the expansion coefficients $\rho_{\mathrm{LL}'}(a, a^\dagger, t)$ are functions of the dynamical variables a, $a^\dagger$ of the laser mode and L, L' label the atomic levels. For real atoms, quite a number of levels may be involved.

It shall suffice to give a brief outline of our analytical and numerical treatment of (1); details can be found in [13]. It is possible to transform eq. (1) into a set of equations that involve only the two laser levels $|\mathrm{A}\rangle$ and $|\mathrm{B}\rangle$ and those pump levels which are connected to $|\mathrm{A}\rangle$ and $|\mathrm{B}\rangle$ via a coherent field [8], [13]. The Ca^+ scheme of fig. 1*b*) can thereby be reduced to three levels in the case of coherent pumping (Ω) and to only two levels for incoherent pumping (Γ). In the latter case, the evolution of ρ_{AA}, for example, is described by

$$\left(\frac{\partial}{\partial t} - L_{\mathrm{cav}} + \gamma_{\mathrm{A}}\right)\rho_{\mathrm{AA}} =$$

$$= -g(\rho_{\mathrm{AB}}a^\dagger + a\rho_{\mathrm{BA}}) + \int_{-\infty}^{t} \mathrm{d}t' \left[R^{\mathrm{eff}}_{\mathrm{AA}}(t-t')\rho_{\mathrm{AA}}(t') + R^{\mathrm{eff}}_{\mathrm{BA}}(t-t')\rho_{\mathrm{BB}}(t')\right], \tag{2}$$

where g denotes the coupling strength between the laser transition and the cavity mode, γ_{A} the sum of all relaxation rates out of the level $|\mathrm{A}\rangle$. Equation (2) and the corresponding equations

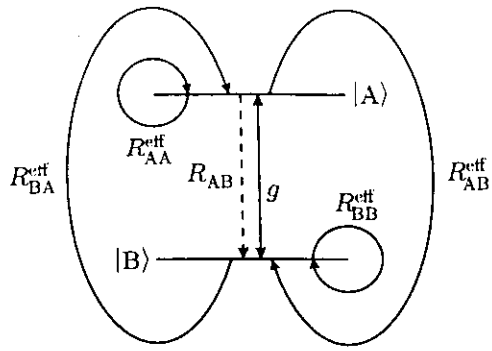

Fig. 2. – Effective two-level system interacting with a non-Markovian (hot) reservoir.

for $\rho_{\rm BB}$, $\rho_{\rm AB}$ and $\rho_{\rm BA}$ describe a two-level laser which, in effect, interacts with a non-Markovian reservoir as depicted in fig. 2. The integral kernels $R^{\rm eff}_{\rm LL'}(\tau)$ are operators that summarize the details of the pump process from level L to L' (L, L' = A, B), which may involve any number of intermediate levels. Note that these kernels depend on the time difference $\tau = t - t' \geq 0$. Every transition into a pump level removes the ion for some time τ from the direct coupling to the laser field until it is excited back to the laser levels. This is indicated by the loops in fig. 2. In the Ca^+ scheme of fig. 1*b*), for example, we choose $|4\,P_{1/2}\rangle$ and $|3\,D_{3/2}\rangle$ as $|{\rm A}\rangle$ and $|{\rm B}\rangle$, respectively. For incoherent pump fields, the loop from $|{\rm B}\rangle$ to $|{\rm A}\rangle$, described by the operator $R^{\rm eff}_{\rm BA}$ in fig. 2, summarizes the pump channels $3\,D_{3/2} \to 4\,P_{3/2} \to 4\,S_{1/2} \to 4\,P_{1/2}$ and $3\,D_{3/2} \to 4\,P_{3/2} \to 3\,D_{5/2} \to 4\,P_{3/2} \to 4\,S_{1/2} \to 4\,P_{1/2}$. The time delay due to pumping via intermediate levels introduces a certain memory effect into the dynamics. In steady state, the time integrals in (2) are replaced by time-independent pump operators $R^{\rm eff}_{\rm LL'} = \int_0^\infty {\rm d}\tau\, R^{\rm eff}_{\rm LL'}(\tau)$. An explicit expression for such a pump operator has been given in [8] for a four-level system. The resulting set of equations can then be solved via a damping-basis expansion [14] of $\rho_{\rm LL'}$. This expansion has the virtue that both $L_{\rm cav}$ and the pump operators $R^{\rm eff}_{\rm LL'}$ are diagonal in that basis, which simplifies the numerical treatment substantially. A discussion of the damping-basis treatment of coupled density-matrix equations can, *e.g.*, be found in [6], [13].

After this sketch of the mathematical treatment of the master equation (1), we now discuss the experimental preliminaries. A single ion can be trapped much easier and longer than a single atom, for example in an endcap trap [15], whose open geometry leaves room for an optical resonator and the application of pump fields, see fig. 1*a*). We have studied several ions as candidates. However, most of the ions do not meet the required conditions. First, the transition between the ground state and the lowest excited state has usually too short a wavelength to be accessible for conventional lasers. Singly ionized alkaline-earth ions possess only one outer electron and therefore seem to be most promising. Second, the spontaneous decay rate $R_{\rm AB}$ on the lasing transition has to be small enough for stimulated emission to prevail, but large enough to ensure a strong atom-field coupling. Finding the right balance is one of the problems one has to deal with in the search for a working experimental scheme.

We here propose to use a $^{40}Ca^+$ ion. (Other candidates are Sr^+ and Ba^+, which have a similar level structure.) The relevant energy levels and dipole-allowed transitions are depicted schematically in fig. 1*b*), the corresponding spontaneous decay rates and wavelengths are listed in table I. The ion is pumped coherently from the ground state to the upper laser level $4\,P_{1/2}$. Stimulated emission into the resonator mode takes place on the transition to $3\,D_{3/2}$, which has a wavelength $\lambda = 866\,{\rm nm}$ [16]. Thereby, a Λ configuration is realized. The pump fields Γ_1 and Γ_2 are needed to close the pump cycle and to depopulate the metastable levels $3\,D_{3/2}$

TABLE I. – *Transition rates and wavelengths for* Ca^+ [17].

Transition	Rate (10^8 s^{-1})	Wavelength (nm)
$4\,^2S_{1/2}$ – $4\,^2P_{1/2}$	1.4	396.85
– $4\,^2P_{3/2}$	1.47	393.37
$3\,^2D_{3/2}$ – $4\,^2P_{1/2}$	0.106	866.21
– $4\,^2P_{3/2}$	0.0111	849.80
$3\,^2D_{5/2}$ – $4\,^2P_{3/2}$	0.099	854.21

and $3\,D_{5/2}$. The nuclear spin vanishes for the chosen isotope of calcium so that there is no hyperfine structure that can complicate the situation.

We assume the resonator mode and the coherent pump field (Ω) to be linearly polarized and the incoherent pump fields (Γ_1 and Γ_2) to be unpolarized. As a consequence, each of the Zeeman manifolds $3\,D_{3/2}$, $3\,D_{5/2}$ and $4\,P_{3/2}$, whose sublevels are labeled by their magnetic quantum number m_J, has to be subdivided into two levels. Therefore our Ca^+ scheme involves eight levels. With the help of the pump-operator approach sketched above, the system can be reduced to three coherently coupled levels: the upper laser level $|\mathrm{A}\rangle = |4\,P_{1/2}\rangle$, the lower laser level $|\mathrm{B}\rangle = |3\,D_{3/2}, m_J = \pm 1/2\rangle$ and the pump level $|\mathrm{C}\rangle = |4\,S_{1/2}\rangle$.

Two of the parameters that enter the description of the one-atom laser depend on the given resonator: the cavity decay rate A and the atom-field coupling strength g. We consider an open optical resonator with its fundamental TEM_{00} mode (with waist w_0) being in resonance with the atom. The resonator is characterized by its finesse $\mathcal{F}$, its length L, and the curvature of its mirrors. The cavity damping rate and the coupling strength are given by

$$A = \frac{\pi c}{L\mathcal{F}} \qquad \text{and} \qquad g = \left(\frac{3c\lambda^2 R'_{\mathrm{AB}}}{8\pi V}\right)^{1/2}, \tag{3}$$

where c is the speed of light. The atom-field coupling depends on the mode volume, which is approximated by $V = \pi w_0^2 L/4$. To achieve a strong coupling with reasonable mirror curvatures, the length of the resonator has to be small. The rate R'_{AB} in (3) accounts for

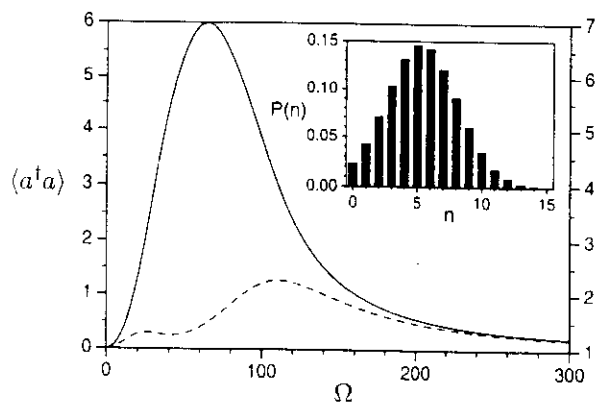

Fig. 3. – Mean photon number $\langle a^\dagger a\rangle$ (solid) and Fano factor F (dashed) *vs.* the coherent pump strength Ω for the Ca^+ scheme. The parameters are $A = 1$, $g = 14.8$, $\Gamma_1 = 40$ and $\Gamma_2 = 100$. The inset shows the photon distribution $P(n)$ for $\Omega = 50$. All rates are in MHz.

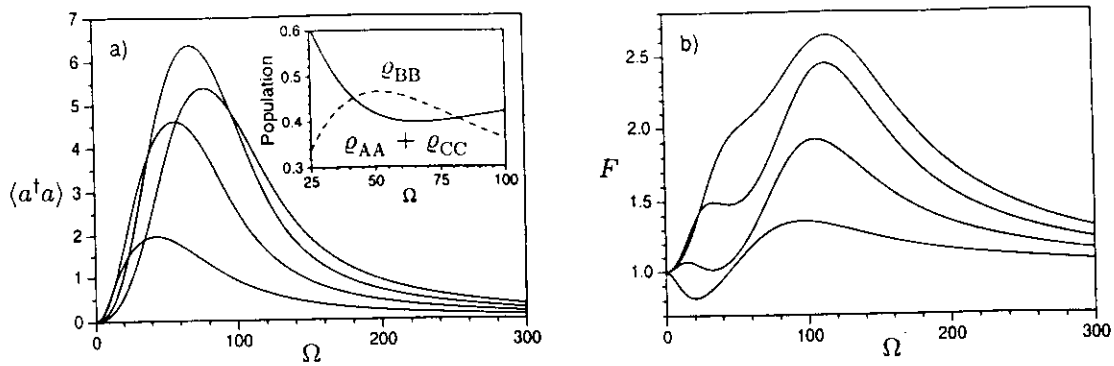

Fig. 4. – *a*) Mean photon number $\langle a^\dagger a\rangle$ and *b*) Fano factor F *vs.* Ω. The curves are for $\Gamma_1 = 5, 20, 60, 120$ (from bottom to top). The inset in *a*) shows the populations in $|A\rangle$ and $|C\rangle$ (solid) and in $|B\rangle$ (dashed) for $\Gamma_1 = 5$. The other parameters are as in fig. 3. All rates are in MHz.

those spontaneous decays on the laser transition that are associated with the polarization of the laser mode. For the calculation, we have chosen the parameters $A = 1\,\mathrm{MHz}$ and $g = 14.8\,\mathrm{MHz}$, which corresponds to a mode volume $V = 0.5 \times 10^{-12}\,\mathrm{m}^3$ and $R'_{AB} = \frac{1}{3} \times 10.6\,\mathrm{MHz}$. These parameters can be realized by using, for example, a symmetric resonator with $L = 1\,\mathrm{mm}$, $w_0 = 25\,\mu\mathrm{m}$ and $\mathcal{F} = 10^6$. The ion should be localized at an antinode of the cavity mode.

Figure 3 demonstrates the possibility of single-atom lasing. In our case the ion-trap laser has two thresholds as a function of the coherent pump strength Ω (defined by a term $\hbar\Omega|A\rangle\langle C| + \mathrm{H.c.}$ in the Hamiltonian). The first threshold is characterized by a maximum in the photon number fluctuations as a function of the coherent pump strength Ω and a linear increase in the mean photon number. This indicates the onset of laser action. With increasing Ω, the mean photon number reaches a maximum before it decreases. At the same time, the Fano factor $F = \langle(a^\dagger a - \langle a^\dagger a\rangle)^2\rangle/\langle a^\dagger a\rangle$, which measures the relative strength of fluctuations in the photon number, goes through a minimum. Here the laser field has a photon distribution $P(n)$ as given in the inset of fig. 3. For even larger values of Ω, there is a second threshold with strong fluctuations and a drop in the intensity, *i.e.* the laser goes out. This behaviour is a consequence of the dynamic Stark shift of the upper laser level.

By variation of the incoherent pump $3D_{3/2} \leftrightarrow 4P_{3/2}$ out of the lower laser level, as illustrated in fig. 4, three phenomena can be observed: i) sub-Poissonian statistics, ii) formation of two thresholds and iii) self-quenching. If in the situation of fig. 3 the pump rate Γ_1 is decreased, the two maxima and the minimum for the Fano factor become more pronounced, see fig. 4*b*). Eventually, the minimum drops below one and the first threshold vanishes, indicating sub-Poissonian statistics ($F < 1$) and thresholdless lasing. It is worth mentioning that for particular values of Ω the laser light is exactly Poissonian, although we are not "far above threshold". If, on the other hand, the pump rate Γ_1 is increased, the two thresholds merge and the mean photon number starts to decrease. For still larger Γ_1, there is no lasing anymore. This behaviour has been called self-quenching [5] and is due to the destruction of the atomic polarization on the lasing transition by the incoherent pump. As noted above, owing to the dynamic Stark effect, there is a similar behaviour for a strong coherent pump.

A remarkable further aspect of this ion-trap laser is given by the fact that it can be operated without population inversion. In the region where lasing occurs, which is around $\Omega = 50\,\mathrm{MHz}$, see fig. 4*a*), the population ϱ_{BB} in the lower laser level can be larger than the sum of the upper-level population ϱ_{AA} and the ground-state population ϱ_{CC} [11]. On the

other hand, for large Ω, the populations on the laser transition are inverted ($\varrho_{AA} > \varrho_{BB}$). Thus, there is lasing without inversion in one region and inversion without lasing in another region [18]. Experimentally, it would be interesting to infer the populations from fluorescence measurements on the involved transitions. It should be noted that for the given transition rates the coherent nature of the pump field Ω is crucial in order to obtain lasing and sub-Poissonian statistics. In the case of only incoherent pumps, to realize population inversion for the given rates in Ca^+, one has to pump so strongly into and out of the laser levels that the self-quenching effect suppresses laser action even before the first threshold can occur.

To summarize, we have investigated the steady-state properties of an ion-trap laser. This would be the first laser operating with only one single atom as the active medium. Sub-Poissonian laser light is predicted. By switching from incoherent to coherent pumping, atomic coherence effects can be demonstrated. Since we have used realistic parameters, our results prepare the ground for a future experiment.

***

The authors thank B.-G. ENGLERT for valuable discussions. H-JB acknowledges financial support by ITAMP at Harvard University and by the Alexander von Humboldt Foundation.

REFERENCES

[1] For laser-cooling techniques, see *Laser Manipulation of Atoms and Ions*, edited by E. ARIMONDO, W. D. PHILLIPS and F. STRUMIA (Elsevier, Amsterdam) 1992.

[2] KIMBLE H. J., in *Cavity Quantum Electrodynamics*, edited by P. R. BERMAN (Academic, Boston) 1994, p. 203.

[3] MESCHEDE D., WALTHER H. and MÜLLER G., *Phys. Rev. Lett.*, **54** (1985) 551; BRUNE M., RAIMOND J. M., GOY P., DAVIDOVICH L. and HAROCHE S., *Phys. Rev. Lett.*, **59** (1987) 1899.

[4] AN K., CHILDS J. J., DASARI R. R. and FELD M. S., *Phys. Rev. Lett.*, **73** (1994) 3375.

[5] MU Y. and SAVAGE C. M., *Phys. Rev. A*, **46** (1992) 5944.

[6] GINZEL C., BRIEGEL H.-J., MARTINI U., ENGLERT B.-G. and SCHENZLE A., *Phys. Rev. A*, **48** (1993) 732.

[7] PELLIZZARI T. and RITSCH H., *J. Mod. Opt.*, **41** (1994) 609; *Phys. Rev. Lett.*, **72** (1994) 3973; HORAK P., GHERI K. M. and RITSCH H., *Phys. Rev. A*, **51** (1995) 3257.

[8] BRIEGEL H.-J., MEYER G. M. and ENGLERT B.-G., *Phys. Rev. A*, **53** (1996) 1143; *Europhys. Lett.*, **33** (1996) 515.

[9] For a recent review, see ARIMONDO E., in *Progress in Optics*, Vol. **XXXV**, edited by E. WOLF (Elsevier, Amsterdam) 1996, p. 257.

[10] KHAZANOV A. M., KOGANOV G. A. and GORDOV E. P., *Phys. Rev. A*, **42** (1990) 3065; RALPH T. C. and SAVAGE C. M., *Phys. Rev. A*, **44** (1991) 7809; RITSCH H., ZOLLER P., GARDINER C. W. and WALLS D. F., *Phys. Rev. A*, **44** (1991) 3361.

[11] GHERI K. M. and WALLS D. F., *Phys. Rev. A*, **45** (1992) 6675; RITSCH H. and MARTE M. A. M., *Phys. Rev. A*, **47** (1993) 2354.

[12] DIEDRICH F. and WALTHER H., *Phys. Rev. Lett.*, **58** (1987) 203; KIMBLE H. J., DAGENAIS M. and MANDEL L., *Phys. Rev. Lett.*, **39** (1977) 691.

[13] MEYER G. M., doctoral thesis, University of Munich, 1996.

[14] BRIEGEL H.-J. and ENGLERT B.-G., *Phys. Rev. A*, **47** (1993) 3311.

[15] SCHRAMA C. A., PEIK E., SMITH W. W. and WALTHER H., *Opt. Commun.*, **101** (1993) 32.

[16] The lowest mirror loss was reported near 850 nm by REMPE G., THOMPSON R. J., KIMBLE H. J. and LALEZARI R., *Opt. Lett.*, **17** (1992) 363.

[17] NIST Database for Atomic Spectroscopy (NIST, Gaithersburg) 1995.

[18] SCULLY M. O., ZHU S.-Y. and GAVRIELIDES A., *Phys. Rev. Lett.*, **62** (1989) 2813.

SPECTROSCOPY OF TRAPPED IONS

H. WALTHER

Sektion Physik der Universität München and
Max-Planck-Institut für Quantenoptik
85748 Garching, Fed. Rep. of Germany

ABSTRACT

In this paper two groups of applications of ion traps will be discussed: those on high precision spectroscopy of single ions and on the investigation of phase transitions of a few ions in traps.

1. Introduction

Ion traps got an important tool for precision spectroscopy. After the pioneering work on single ion spectroscopy performed end of the seventies[1] it got clear that this system allows to observe an ion in an unperturbed environment with practically no influence of the trapping fields. Another advantage is that the interaction time with the laser beam is not limited by the motion of the particle, therefore no transit time broadening is present. The fact that the motion of the ions can be cooled by laser light allows to reach the so-called Dicke limit[2,3] which means that the residual motional amplitude of the ion is much smaller than a fraction of the light wavelength used to probe the resonance line. In this limit the Doppler broadening disappears and since the temperature is in the range of mK or below also the second-order Doppler effect is excluded. Thus the ultimate resolution is determined by the natural lifetime of the investigated transition.

High resolution experiments have also been performed in ion traps in the microwave region. In this case the Doppler effect does not show up due to the low frequency of the investigated transitions and the number of ions stored in the trap can be very large. There is also a lot of work performed on the development of frequency standards in the microwave region; this cannot be covered here (for details see a recent review[4,5]). It should be mentioned here that not all those experiments have to be performed using laser light for the state preparation and detection of the ions. For example one of the early experiments of this kind was the determination of the Zeeman splitting of $^4He^{+6}$ and of the hyperfine splitting of the $^3He^+$ ground state by Schussler et al.[7]. The ions in the trap were polarized by spin exchange collisions with a polarized beam of Cs atoms. The microwave resonance destroyed the polarization of the $^3He^+$ leading to a smaller lifetime of the ions in the trap. Also optical pumping detection using the light of resonance lamps was performed in other cases.

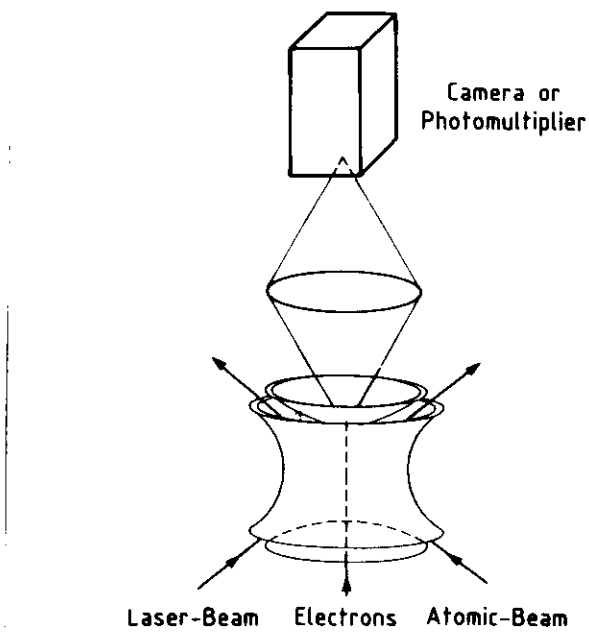

Fig. 1: Scheme of the Paul trap.

2. Spectroscopy of single ions

The Paul-trap[8,9] used for most of the experiments described here consists of a ring electrode and two end caps as shown in Fig. 1. Trapping can be achieved if time-varying electric fields are applied between ring and caps (the two caps are electrically connected). A dc voltage in addition changes the relation of the potential depth along the symmetry axis (vertical direction in Fig. 1) to that in a perpendicular direction. The equation of motion of an ion in such a situation is the Mathieu differential equation, well known in classical mechanics, which – depending on the voltages applied to the trap (dc and radio-frequency voltages) – allows stable and unstable solutions. Another way to achieve trapping is the use of a constant magnetic field aligned along the symmetry axis leading to the Penning trap.[10,11] In this case only a dc voltage has to be applied between ring and cap electrodes.

To produce the ions in the Paul trap mostly a neutral atomic beam is directed through the trap centre and ionized by electrons. The resulting trapped ions have a lot of kinetic energy rendering them useless for most applications, such as spectroscopy; therefore the ions have to be cooled. This is done by laser light. The laser frequency ν is tuned below the resonance frequency, so that the energy of the photon is not sufficient to excite the atom.[3] Crudely, the ion can extract the missing energy from its motion and thus reduce its kinetic energy. In other words, the atomic velocity Doppler

Table 1: Investigation of trapped ions in connection with the test of fundamental quantum phenomena. In the experiments on the linearity of quantum mechanics and on the Zeno effect ion clouds have been investigated.

Phenomenon	References
Antibunching and sub-Poissonian statistics in resonance fluorescence	Diedrich and Walther [13]
Quantum jumps	Nagourney *et al.* [14], Sauter *et al.* [15], Bergquist *et al.* [16]
Interference of the light of two ions	Eichmann et al. [17]
Linearity of quantum mechanics	Bollinger *et al.* [18]
Zeno-effect	Itano *et al.* [19]

Table 2: Potential ions for optical frequency standards.

Ion	Cooling transition	Clock transition	Lifetime clock transition	References
Ba^+	$6p\ ^2P_{1/2}$-$6s\ ^2S_{1/2}$ 493 nm	$5d\ ^2D_{5/2}$-$6s\ ^2S_{1/2}$/1.76 μm	32 s	Neuhauser *et al.* [1] Nagourney *et al.* [23]
Hg^+	$6p\ ^2P_{1/2}$-$6s\ ^2S_{1/2}$ 194 nm	$6d\ ^2D_{5/2}$-$6s\ ^2S_{1/2}$/282 nm	0.1 s	Bergquist *et al.* [21, 24] Diedrich *et al.* [22]
Yb^+	$6p\ ^2P_{1/2}$-$6s\ ^2S_{1/2}$	$6d\ ^2D_{5/2}$-$6s\ ^2S_{1/2}$		Klein *et al.* [25]
		$6f\ ^2F_{7/2}$-$6s\ ^2S_{1/2}$	8d	Bell *et al.* [26] Lehmitz *et al.* [27]
In^+	$5s5p\ ^3P_1$-$5s^2\ ^1S_0$ 230 nm	$5s5p\ ^3P_0$-$5s^2\ ^1S_0$/236 nm	0.13 s	Dehmelt [20] Peik *et al.* [28]
Sr^+	$5p\ ^2P_{1/2}$-$5s\ ^2S_{1/2}$ 422 nm	$4d\ ^2D_{5/2}$-$5s\ ^2S_{1/2}$/674 nm	0.372 s	Madej and Sankey [29]

shifts the atom into resonance to bridge the detuning gap Δ between laser and resonance frequency, and the atom absorbs the photon of momentum $\hbar k = h\nu/c$. After the absorption process the momentum of the atom is reduced, lowering its kinetic energy. The lowest temperature achievable is determined by the Doppler limit,[3,12] which is in the millikelvin region. The low temperatures can be obtained within a fraction of a second.

After the pioneering work of Dehmelt and Toschek on the spectroscopy of single Ba-ions[1] it got clear that single ion spectroscopy will be an important tool for high resolution spectroscopy and also for new frequency standards. A survey on the applications of single ion spectroscopy is given in tables 1 and 2. The applications reach from the investigation of fundamental quantum phenomena to high resolution

spectroscopy with the aim of the development of new frequency standards.

The proposal to use a forbidden optical transition of a single laser-cooled ion stored in a Paul trap as the basis for an optical atomic frequency standard is more than ten years old.[20] Impressive progress has already been achieved along these lines and high resolution laser spectroscopy has been reported on Hg^+[21,22] and Ba^+ ions.[23] Other ions that are investigated in this context are ytterbium, indium and strontium (see table 2 for a survey). A severe restriction in the choice of ions for these experiments is the availability of suitable transitions: a strong dipole transition is needed for laser cooling and a long lived transition for the frequency standard and both lines have to be in the wavelength range accessible for continuous wave laser sources. The prospective clock transitions of all the ions mentioned above are electric quadrupole transitions like $^2S_{1/2} \rightarrow {}^2D_{5/2}$ or higher order multipole processes. The dependence of those transitions on external electric and magnetic fields may cause a problem for a frequency standard. Around zero magnetic field they show a linear Zeeman shift of the order MHz/G unless a Zeeman component $(m_F = 0) \rightarrow (m_F = 0)$ of an isotope with half integer nuclear spin is used.[21] In this case however the hyperfine splitting of the ground state leads to optical pumping which makes a continuous excitation for laser cooling more complicated. A small but difficult controllable shift arises from the interaction with the electric quadrupole field of the trap.[20]

To avoid these problems Dehmelt suggested the use of a transition between two states with vanishing angular momentum of the electrons such as $6s^2\ {}^1S_0 \rightarrow 6s6p\ {}^3P_0$ in Tl^+[20,30] or the corresponding lines of the other ions of the third main group of the periodic system: boron, aluminium, gallium and indium. The three lighter of these cannot be laser cooled presently because the intercombination line $^1S_0 \rightarrow {}^3P_1$ is too weak and the wavelength of the strong dipole transition $^1S_0 \rightarrow {}^1P_1$ lies in the VUV below 160 nm and is thus inaccessible for cw lasers. In the case of thallium the wavelengths for $^1S_0 \rightarrow {}^3P_0$ and $^1S_0 \rightarrow {}^3P_1$ are 202.2 nm and 190.8 nm respectively, and for indium they are 236.5 nm and 230.6 nm. The two indium wavelengths can be generated relatively easily using the β-bariumborate (BBO) crystal for the fequency doubling of blue lasers. Especially the clock transition at 236.5 nm is technically convenient, since it coincides with the fourth harmonic of the 946 nm transition $^4F_{3/2} \rightarrow {}^4I_{9/2}$ of the Nd:YAG laser. So this intrinsically frequency stable solid-state laser can be used as the oscillator to drive the clock transition. Indium is thus presently the most promising of the group III ions. The possibilities to use this ion for an optical frequency standard are presently investigated in our laboratory.[28] The results obtained so far will be reported in the following.

The decay $^3P_0 \rightarrow {}^1S_0$ between two levels with vanishing electronic angular momenta is forbidden in all orders of the multipole expansion of the radiation field. However for atoms with nonvanishing nuclear spin the hyperfine interaction induces a weak electric dipole transition between these states. This is due to small admixtures of the decaying states $^1P_1$ and $^3P_1$ to the otherwise stable $^3P_0$ level. This effect has been quantitatively investigated so far only in a few cases. In mercury the absorption coefficient for the forbidden transition was measured and the lifetime of $^3P_0$ was inferred from that.[31] The result was 1.7 s for ^{199}Hg and 2.6 s for ^{201}Hg. Recently

lifetimes in the picosecond range have been measured for hyperfine quenched $^3P_0$ states of highly charged helium-like ions.[32] In the experiment reported here we use the perturbation free environment offered by an ion trap to measure the lifetime of the $^3P_0$ state in In^+. We observe the quantum jumps of a single ion into and out of this level using Dehmelt's electron shelving scheme.[20]

For the experiments with single laser-cooled ions a Paul-Straubel-trap with a 1 mm diameter ring electrode was used,[33] driven by a voltage of 1000 V at 10.7 MHz. Together with a small indium oven, an electron source for ionization and the detection optics for monitoring the fluorescence of the ions, the trap is mounted inside a stainless steel ultrahigh vacuum chamber.

The vacuum chamber is surrounded by three pairs of coils oriented along orthogonal axes, one of which coincides with the laser beam direction. These coils are used to compensate for the earth's magnetic field or to apply a controllable magnetic field. When the ions are optically pumped and the fluorescence intensity is observed as a function of the magnetic field, we get a narrow zero field resonance due to magnetic depolarisation of the ground state, analogous to the Hanle effect of an excited state.[34] This signal can be used to cancel magnetic stray fields inside the trap with a precision of a few mG.

The used Paul-Straubel trap produces a steep potential for a good localization of the stored ion and simultaneously the laser straylight is very small owing to the open electrode structure.[33] Without damping through a buffergas the trap still can store several ions but at a typical well depth of 4 eV these can be evaporated from the trap by heating them with the laser detuned to the blue side of the resonance. After this procedure usually a single ion remains which is then trapped with high stability; it can be kept for hours even when it is not permanently laser cooled. We also observed Coulomb crystals[35] of two laser cooled indium ions separated by $3\mu m$.

In order to laser cool the ion on the narrow $^1S_0 \rightarrow {}^3P_1$ transition its hyperfine component $F = \frac{9}{2} \rightarrow \frac{11}{2}$ was excited with circular polarized light in zero magnetic field. This effectively prepares a two level system $(F = m_F = \frac{9}{2}) \rightarrow (F = m_F = \frac{11}{2})$ by means of optical pumping. We observed photon count rates up to 1.2 kHz from a single ion in saturation, indicating that our overall detection efficiency is about 0.1 %. Usually we worked below saturation to get a better ratio of fluorescence signal to laser straylight, where we achieved a value of 12. By scanning the laser we recorded excitation spectra of the cooling transition with a linewidth of about 20 MHz. This is limited partly by laser frequency jitter and also to a larger extent by frequency modulation caused by the micromotion of the ion at the trap frequency of 10.7 MHz. A linewidth of 20 MHz corresponds to a modulation index of 2 and a residual micromotion amplitude of 70 nm that might be caused by a slight displacement ($\approx 1\mu m$) of the ion from the trap center. Very precise control of stray DC fields is required to minimize this effect. The presence of micromotion sidebands leads to a strong variation in the temperature as the laser is scanned across the line profile so that we can presently only give an upper limit of 100 mK for the temperature. If the

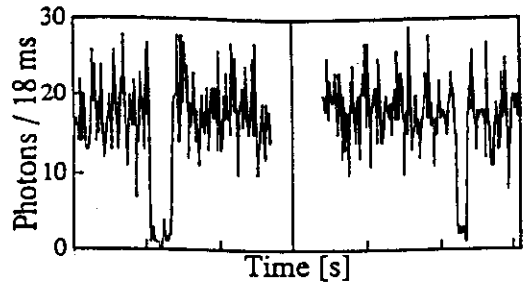

Fig. 2: Fluorescence from a single indium ion, showing dark periods due to quantum jumps to the metastable $^3P_0$ state.

laser frequency is stabilized to a linewidth below the natural linewidth of the cooling transition corresponding to 360 kHz and the micromotion further reduced then much lower temperatures will be feasible.

If we look at the temporal behaviour of the resonance fluorescence of a single indium ion on the transition $^1S_0 \stackrel{1}{\rightarrow} {}^3P_1$ we observe dark periods whenever the metastable $^3P_0$ level is populated. This can happen either by direct laser excitation from the ground state, as it will be done for the frequency standard, or through a magnetic dipole decay from the $^3P_1$ level. The possibility of observing quantum jumps in such a three level system with only one driven transition has been discussed theoretically (see e.g. Ref. 36) and has been realized for the Hg^+ ion[37] (see also table 1 for more references).

In a simple rate equation model let A_0 be the decay rate from $^3P_0 \rightarrow {}^1S_0$, A_1 that from $^3P_1 \rightarrow {}^1S_0$ and A_2 that from $^3P_1 \rightarrow {}^3P_0$. Since $A_1 \gg A_0, A_2$ the fluorescence intensity switches from "on" $\sim A_1\rho_{11}$ (ρ_{11} : population of $^3P_1$) to "off" at a rate $A_2\rho_{11}$ and back "on" at the rate A_0. The magnetic dipole decay rate A_2 for the transition $^3P_1 \rightarrow {}^3P_0$ at $\lambda = 9.32\mu m$ wavelength can be estimated as:[38]

$$A_2 = \frac{2\pi\sigma^2 h}{9\epsilon_0 m^2 c^2 \lambda^3} = 0.0223 s^{-1}$$

The branching ratio A_1/A_2 is about 10^8 and with beginning saturation of the cooling transition ($\rho_{11} = 0.25$) we expect one $^3P_1 \rightarrow {}^3P_0$ decay every 3 minutes.

To observe these dark periods in the experiment we counted the photomultiplier pulses in time intervals of 18 ms and stored these numbers in the computer. The laser power was measured synchronously and checked to be constant. Samples of these data exhibiting quantum jumps are shown in Fig. 2. We see an abrupt decrease of the count rate to the stray light level and the reappearance of the fluorescence after some 100 ms. These events occur at a rate that is a little lower but still consistent with the estimate given above. The duration of the dark periods can be used to evaluate the lifetime of the $^3P_0$ level. We observed about 150 decays and calculated from those data the function $d(t)$ as the number of dark periods with a duration shorter than t. This function was fitted to $d(t) = a(1 - e^{-(t-t_o)/\tau})$ to get the lifetime τ. Events with a duration shorter than $t_o = 70ms$ were not considered. Fig. 3 shows a logarithmic If the

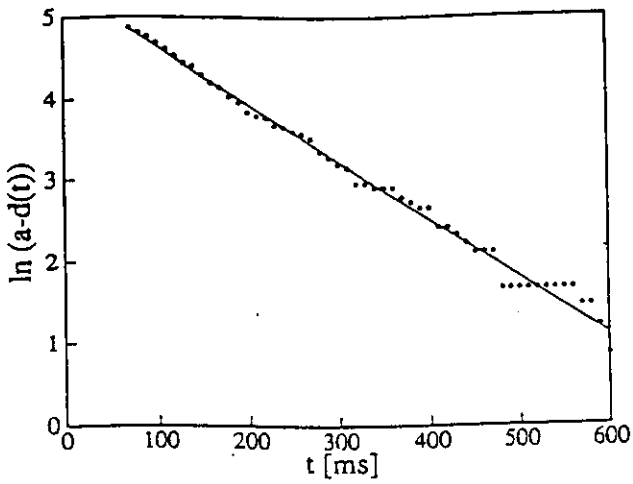

Fig. 3: Distribution of the durations of observed dark periods (see text for the definition of $a - d(t)$). The fitted decay constant is the inverse lifetime of the $^3P_0$ level.

plot of $a - d(t) = ae^{-(t-t_o)/\tau}$ together with the fit, indicating a simple exponential behaviour. The result for the lifetime of $^3P_0$ is

$$\tau\,(^3P_0) = 0.14(2)s.$$

The uncertainty results from the number of observed decays.

The experiments show that the indium ion is a possible candidate for an optical frequency standard. Although the cooling transition in indium is a relatively slow intercombination line with only 360 kHz natural linewidth we were able to cool a single ion using this transition and to obtain a rate of fluorescence photons that is high enough to detect the dark periods due to electron shelving in the $^3P_0$ level. Besides these technical difficulties the small linewidth of the cooling transition enabled us to reach the strong binding regime using moderate trapping field strength. This opens the possibility of cooling the ion into low quantum levels or even the ground state of the single ion oscillator.

A frequency standard will benefit from the insensitivity of the indium ion's $^1S_0 \rightarrow {}^3P_0$ transition frequency against external perturbations as well as from the availability of a frequency stable oscillator like a diode laser pumped Nd:YAG laser. A suitable source has been developed in our laboratory for this purpose. The accuracy to which the wavelength of this forbidden transition is known has recently been improved significantly by the measurement of Larkins and Hannaford,[39] so that direct laser excitation shall be possible in the near future.

3. Observation of phase transitions in a Paul trap - Order versus chaos: crystal versus cloud

In the next part of the paper we would like to describe experiments on phase

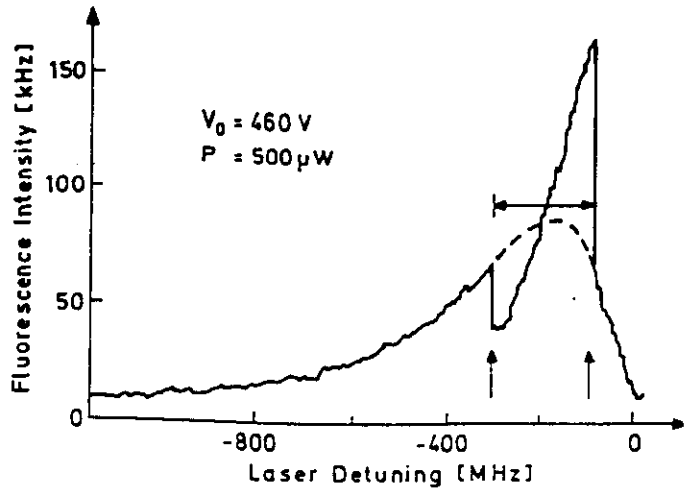

Fig. 4: Fluorescence intensity, that is, photon counts per second, from five ions as a function of the laser detuning Δ. The vertical arrows indicate the detunings where phase transitions occur. The horizontal arrow shows the range of detunings in which a stable five-ion crystal is observed. The spectrum was scanned from left to right.

transitions of a few ions in a Paul trap. The results discussed were obtained using a Paul trap with a ring diameter of 5 mm and an end-cap separation of 3.54 mm.[13,40] This trap is larger than most of the other ion traps used in laser experiments.[1,22] The radio frequency of the field used for dynamic trapping is 11 MHz. The trap is mounted inside a stainless steel, ultrahigh vacuum chamber. The ions are loaded into the trap by means of a thermal beam of neutral atoms (magnesium atoms in our case), which are then ionized close to the center of the trap through a small hole in the lower end-cap (see Fig. 1). In order not to distort the trap potential, the hole is covered by a fine molybdenum mesh. The neutral Mg beam and the laser beam pass through the gaps between the end-cap and the ring electrodes. The laser frequency is shifted by an amount Δ below the $3S_{1/2} \rightarrow 3P_{3/2}$ resonance-transition of $^{24}Mg^+$ at 280 nm to extract kinetic energy from the ions by radiation pressure as discussed previously. In this way, a single ion can be cooled to a temperature below 10 mK. The fluorescence from the ions is observed through a hole in the upper end-cap (see Fig. 1), again covered by a molybdenum mesh. The large size of the trap allows a large solid angle for detecting the fluorescence radiation, either with a photomultiplier, or by means of a photon-counting imaging system. To observe the ions, the cathode of the imaging system is placed in the image plane of the microscope objective attached to the trap; in this way images of the ions could be obtained.[41,42]

The existence of phase transitions in a Paul trap manifests itself by significant jumps in the fluorescence intensity of the ions as a function of the detuning Δ between the laser frequency and the atomic transition frequency. These discontinuities are indicated in Fig. 4 by vertical arrows, and occur between two types of spectra: a broad and a narrow one, analogous to the fluorescence spectrum of a single, cooled ion. We interpret the broad spectrum as a fingerprint of an ion cloud and the narrow

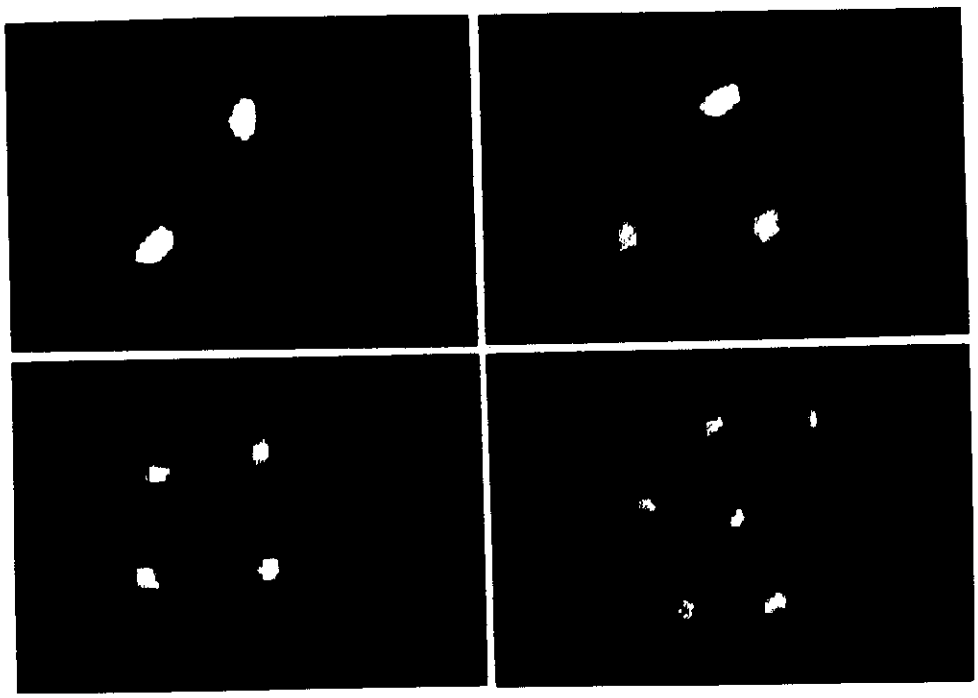

Fig. 5: Two, three, four and seven ions confined by the dynamical potential of a Paul trap and crystallized into an ordered structure in a plane perpendicular to the symmetry axis of the trap. The average separation of the ions is 20 μm.

spectrum as being characteristic for an ordered many-ion situation with a "single-ion signature". Thus the jumps clearly indicate a transition from a state of erratic motion within a cloud to a situation where the ions arrange themselves in regular structures. In such a crystalline ion structure the mutual Coulomb repulsion is compensated by the external, dynamic trap potential. The regime of detunings in which such crystals exist is depicted in Fig. 4 by the horizontal arrow. The existence of the two phases - crystal and cloud - can be verified experimentally by direct observation with the help of a highly sensitive imaging system and theoretically by analyzing ion trajectories via Monte Carlo computer simulations.[42]

The excitation spectrum of Fig. 4 and the jumps in it were recorded by altering the detuning Δ from large negative values to zero. When we scan the spectrum in the opposite direction the jumps occur at different values of Δ, which means hysteresis is associated with these phase transitions.[42] Such hysteresis behavior can be expected with laser-cooled ions because the cooling power of the laser strongly depends upon the details of the velocity distribution of the ions. The behavior of the ions in the trap is governed by the trap voltage, the laser detuning and the laser power. Hysteresis loops appear whenever one of these parameters is changed up or down while the others are kept constant.

Figure 5 shows the ion structures as measured with the imaging system. For the measurements only a radio-frequency voltage was applied to the trap electrodes:

in this case the potential is a factor of two deeper along the symmetry axis than perpendicular to it, and therefore plane ion structures are observed being perpendicular to the symmetry axis.[41,42]

After we have accepted the existence of the ion crystals and the corresponding phase transitions, how do they actually occur? Would the cooling laser not force any cloud immediately to crystallize? A heating mechanism balancing the cooling effect of the laser must be the answer to this puzzle, but what heating mechanism? Since the early days of Paul traps this so-called radio-frequency heating has repeatedly been cited.[3,10] A deeper understanding, however, was missing and was provided only recently by a detailed study of the dependence of the cloud $\rightarrow$ crystal and crystal $\rightarrow$ cloud phase transitions on the relevant parameters.[41–43]

The ions are subjected to essentially four different forces: the first one arising from the trapping field, then the Coulomb interaction between the ions, the laser cooling force, and finally a random force arising from the spontaneously emitted photons. Using these forces computer simulations of the motion of the ions can be performed.[42] Depending on the external parameters such as the laser power, the laser detuning, and the radio-frequency voltage, the experimentally observed phenomena could be reproduced.[42,43] Some of the results of the simulations are summarized in Fig. 6. Plotted is the radio-frequency heating parameter κ of five ions versus their mean separation.[43] For zero laser power and large r, we did not observe any net heating of the ions. This is confirmed by our experiments in which, even in the absence of a cooling laser, large clouds of ions can be stored in a Paul trap over several hours without being heated out of the trap. When the ions are far apart, the Coulomb force is small, and on short time scales the ions behave essentially like independent single stored ions. For this reason, we call this part of the heating diagram the *Mathieu regime*.[41,43] Turning on a small laser, the rms radius r reduces drastically, but comes to a halt at about 14 μm. At this distance the nonlinear Coulomb force between the ions plays an important role and the motion of the ions gets chaotic. In this situation the power spectrum of the ions becomes a continuum leading to a radio-frequency heating process.

Increasing the laser power further results in an even smaller cloud. The smaller cloud produces more chaotic radio-frequency heating, as seen clearly by the negative slope of the heating curve in the range $8<r<14$ μm. Finally, in the range $4<r<8$ μm there is still chaotic heating but the slope of the heating curve is positive. As a consequence of the resulting triangular shape of the heating curve at a laser power of about $P = 150$ μW, corresponding to $r \approx 8$ μm, the chaotic heating power can no longer balance the cooling power of the laser light and the cloud collapses into the crystalline state located at $r \approx 3.8$ μm. At this point the amplitude of the ion motion is so small that the nonlinear part of the repulsive Coulomb force is negligible again, so that chaotic heating disappears and the phase transition occurs.

Due to this collapse of the cloud state, the behavior of the heating rate in the range $3.8<r<8$ μm cannot be studied by balancing laser cooling and radio-frequency heating. In this case we start out from the crystal state and slightly displace the ions to explore the vicinity of the crystal. We observe no heating for $3.8<r<4$ μm, but

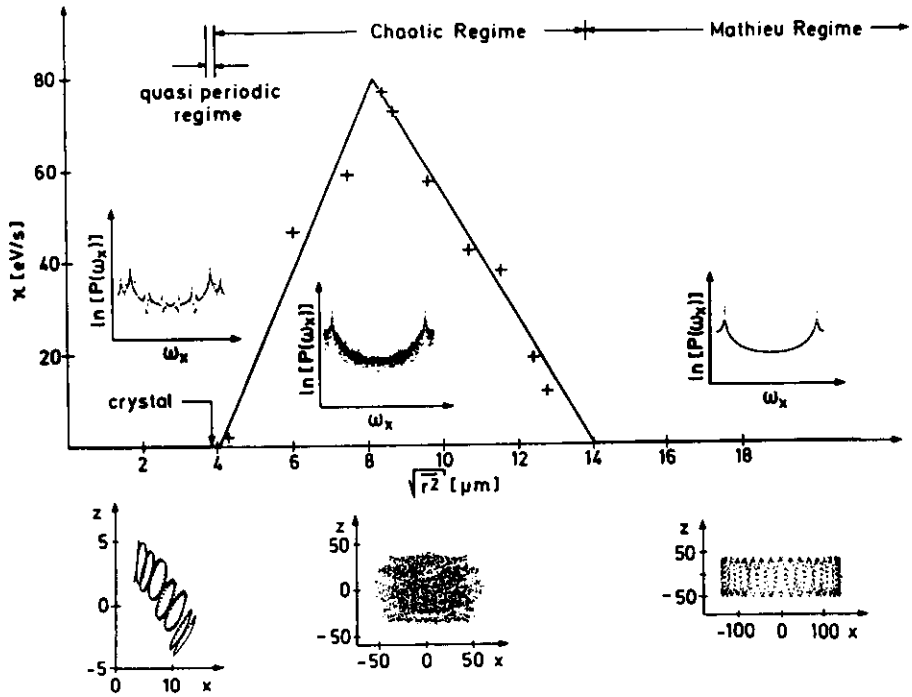

Fig. 6: Average heating rate κ (increase of kinetic energy per unit time), of five ions in a Paul trap versus mean ion separation. The insets show the power spectrum and the corresponding stroboscopic Poincaré sections (plane perpendicular to the symmetry axis) of relative separation of the two ions in three characteristic domains: The crystal state, the chaotic regime, and the Mathieu-regime. The units on the axes are in μm. In order to calculate the power spectrum of the "crystal" shown on the left hand side, the distance of the two ions was displaced by 1 μm from the equilibrium position. The Mathieu-regime shown on the right is dominated by the secular motion.

quasiperiodic motion, and thus dub this the *quasiperiodic regime*. We call the upper edge of the quasiperiodic regime ($r \approx 4$ μm) the *chaos threshold*. An initial condition beyond the chaos threshold, i.e., satisfying $r \approx 4$ μm, leads to heating, and expansion of the ion configuration.

For the quasiperiodic, the chaotic, and the Mathieu regimes, respectively, we display the corresponding type of power spectrum as the insets above the abscissa of Fig. 6. The data were actually taken for the case of two ions, but would not look much different in the five-ion case. We obtain a discrete spectrum in the quasiperiodic regime and a complicated noisy spectrum in the chaotic regime. The spectrum in the Mathieu regime is again quite simple and dominated by the secular motion frequency. We also show stroboscopic pictures of the locations of the ions in the plane perpendicular to the symmetry axis of the trap characterizing the three regions (inserts below the abscissa in Fig. 6).

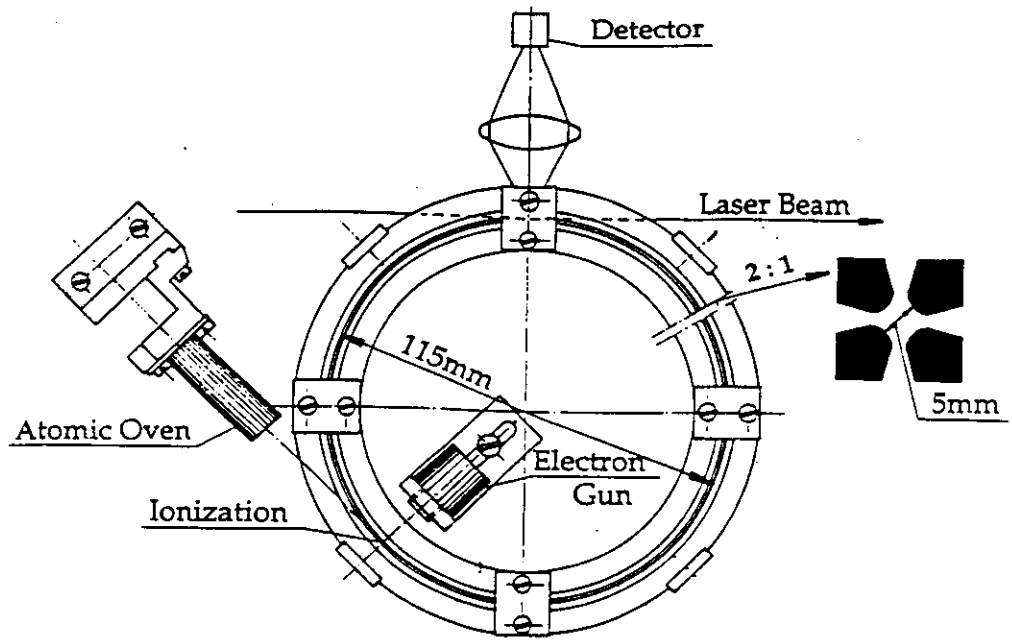

Fig. 7: Quadrupole storage ring. The cross section of the electrode configuration is shown on the insert on the right hand side of the figure.

4. The ion storage ring

A completely new era of accelerator physics could begin if it were possible to produce, store and accelerate Coulomb crystals in particle accelerators and storage rings. To work with crystals instead of the usual dilute, weakly coupled particle clouds has at least one advantage: the luminosity of accelerators (storage rings) could be greatly enhanced and (nuclear) reactions whose cross sections are too small to be investigated in currently existing accelerators would become amenable to experimentation.

In the following, we would like to discuss very briefly our experiments using a miniature quadrupole storage ring. The storage ring is similar to the one described by Drees and Paul[44] or by Church.[45] We can observe phase transitions of the stored ions and the observed ordered-ion structures are quite similar to the ones expected in relativistic storage rings, however, much easier to achieve. The motivation for building this small storage ring came from the fact that micromotion perturbs the ion structures in a Paul trap and only a single trapped ion is free of micromotion.[3] The ring trap used consists of a quadrupole field, leading to harmonic binding of the ions in a plane transverse to the electrodes of the quadrupole and no confinement along the axis (see Fig. 7). Confinement along the axis is achieved, however, by the Coulomb interaction between the ions when the ring is filled; then the total number of ions in the ring determines the average distance between them.

A scheme of the ring trap used for our experiment is shown in Fig. 7.[46,47] It consists of four electrode rings shown in the insert on the right. The hyperbolic

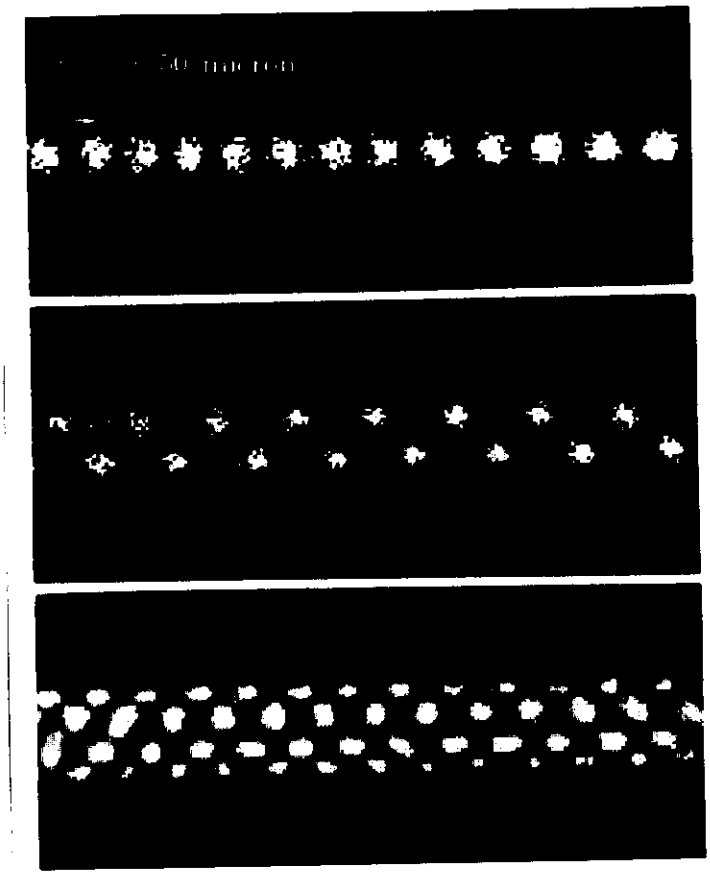

Fig. 8: Crystalline structures of laser-cooled $^{24}Mg^{+}$ ions in the quadrupole storage ring. At a low ion density ($\lambda = 0.29$) the ions form a string along the field axis (a, upper). Increasing the ion density transforms the configuration to a zigzag (b, middle; $\lambda = 0.92$). At still higher ion densities, the ions form ordered helical structures on the surface of a cylinder, e.g., three interwoven helices at $\lambda = 2.6$ (c, lower). As the fluorescent light is projected onto the plane of observation in this case the inner spots are each created by two ions seated on opposite sides of the cylindrical surface, resulting in a single, bright spot.

cross section of the electrodes required for an ideal quadrupole field was approximated by a circular one. The experiments were also performed with Mg^{+} ions. The ions were produced between the ring electrodes by ionizing the atoms of a weak atomic beam produced in an oven that injected the atoms tangentially into the trap region. The electrons used for the ionization came from an electron gun, the electron beam of which was perpendicular to the direction of the atomic beam. A shutter in front of the atomic beam oven allowed the interruption of the atomic flux. The ultrahigh vacuum chamber was pumped by an ion getter pump. After baking the chamber a vacuum of 10^{-10} mbar could be reached. Under these conditions the number of ions stored in the trap stayed practically constant for several hours.

When laser cooling of the ions is started a sudden change in the fluorescence intensity is observed, resembling very much that seen with stored ions in a Paul trap (Fig. 4), which indicates a phase transition and the formation of an ordered structure of ions. The ion structure can also be observed using an ultrasensitive imaging system. Pictures of typical ion structures are shown on Fig. 8. The ions are excited by a frequency-tunable laser beam that enters the storage ring tangentially.

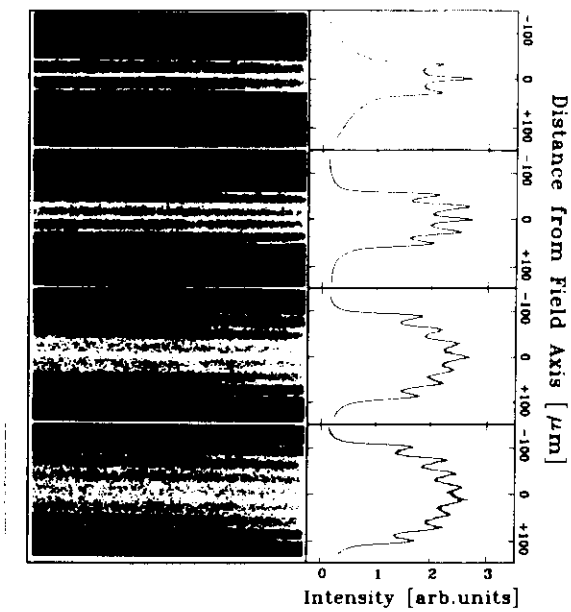

Fig. 9: Images and intensity profiles of (from the top): one shell plus string (a; $\lambda \approx 4.3$), two shells plus string (b: $\lambda \approx 12.2$), three shells plus string (c; $\lambda \approx 26$), and four shells (d; $\lambda \approx 34$). There are up to $\approx 8 \times 10^5$ ions stored in the ring for the four-shell structure.

In the linear configuration the ions are all sitting in the center of the quadrupole field, therefore they do not show micromotion and it is possible to cool them further to temperatures in the microkelvin region. The new cooling methods proposed by Dalibard et al.[12] can be applied to the Mg^+ ions so that the single-photon recoil limit can be achieved for the cooling process. At this limit the kinetic energy of the ions is smaller than the energy resulting from the "zero-energy" motion of the harmonically bound ions; the ion structure then reaches its vibrational ground state, i.e. a Mössbauer situation is generated. That means that the recoil limit for laser cooling of the ions does not exist anymore, the ion structure then corresponds to a Wigner crystal.

The observed configurations (Figs. 8 and 9) in the quadrupole ring trap are described in a recent paper by Birkl et al.[48] We will review the major results reported in that paper in the next section as well as the comparison to the theory (Rahman and Schiffer;[49] Hasse and Schiffer[50]).

In the molecular dynamics calculations,[50] a cylindrically symmetric, static harmonic potential is assumed to describe the confining field. Each particle is subjected to the Coulomb forces of all other particles and to the confining field. The classical equations of motion are integrated for a system of several thousand particles, starting with random positions and velocities, to give the time evolution of the system. Cooling the stored particles is simulated by scaling down the resulting velocities of the stored particles at defined instants of the integration process. After sufficient cooling, ordered structures such as strings, zigzags, shells and multiple shells should arise,

owing to the confining field's harmonic potential. Our experiments are well suited to checking these predictions. To compare the experimental results with theory, we can use the normalized "linear particle density" λ, which is given by the ion density multiplied by the ratio of Coloumb repulsion and confining force of the trap.[50] Low λ values correspond to a deep potential well or a small number of ions, resulting in an equilibrium structure closely confined to the field axis making up a string of ions (Fig. 8a). This is the micromotion-free configuration discussed previously, and the analogue of the single stored ion in a Paul trap, as in both cases the ions sit in the potential minimum and show no micromotion. For higher values of λ, the structures extend more and more into the off-axis region, giving rise to (in the order of increasing λ) a plane zigzag structure (Fig. 8b) and cylindrical structures with the ions forming helices on cylindrical surfaces. The structure in Fig. 8c consists of three interwoven helices with six ions per pitch. The string and the zigzag have also been observed with laser-cooled Hg^+ ions in a linear trap.[51]

Increasing further the number of ions leads to structures with smaller spacings between the ions where we cannot optically resolve individual ions any more. Images of these structures are presented in Fig. 9. The radial intensity profiles displayed on the right-hand side of the figure provide information about the structures as they give a measure of the radial distribution of the ions. For increasing λ it becomes energetically more favourable to create a string inside the first ion shell (Fig. 9a) to provide space for more particles. This results in a structure that is a three-dimensional analogue of the plane seven-ion crystal for a Paul trap (Fig. 5). The inner string turns into a second shell at higher densities: a string then develops inside this second shell (Fig. 9b), and so on. Figures 9c and 9d show structures consisting of three shells plus string, and four shells, respectively. We have been able to observe all possible structures, from the string up to four shells plus string. The formation of multiple-shell crystalline structures in the quadrupole storage ring contrasts with the observation of shell structures in Penning traps, where the ions do not occupy fixed positions inside the shells.[52]

Figure 10a gives a summary of experimental data for all recorded images in which the ions were individually resolved. The depth of ψ_o of the potential well and the ion density per unit length are the experimental parameters. The theoretical boundaries between the different shell structures, predicted by Hasse and Schiffer[50] in terms of the functional dependence of λ on ψ_o and the ion density are given by the straight lines with constant λ. String structures are expected for $\lambda < 0.709$, zigzag structures in the range $0.709 < \lambda < 0.964$ and single shells in the range $0.964 < \lambda < 3.10$. Many different structures that are degenerate in energy are expected within the single-shell regime. We obtained stable configurations near $\lambda = 1.3$ and $\lambda = 2.0$ (two interwoven helices) and near $\lambda = 3.0$ (three interwoven helices - Fig. 8c). The observed structures agree with the predicted scheme for a large range of experimental parameters, thus confirming the theoretical results.

A summary of the experimental observations for ordered-shell structures with up to four shells plus string and without resolution of individual ions is presented in Fig. 10b. The depth ψ_o of the confining potential well is again one of the experimental

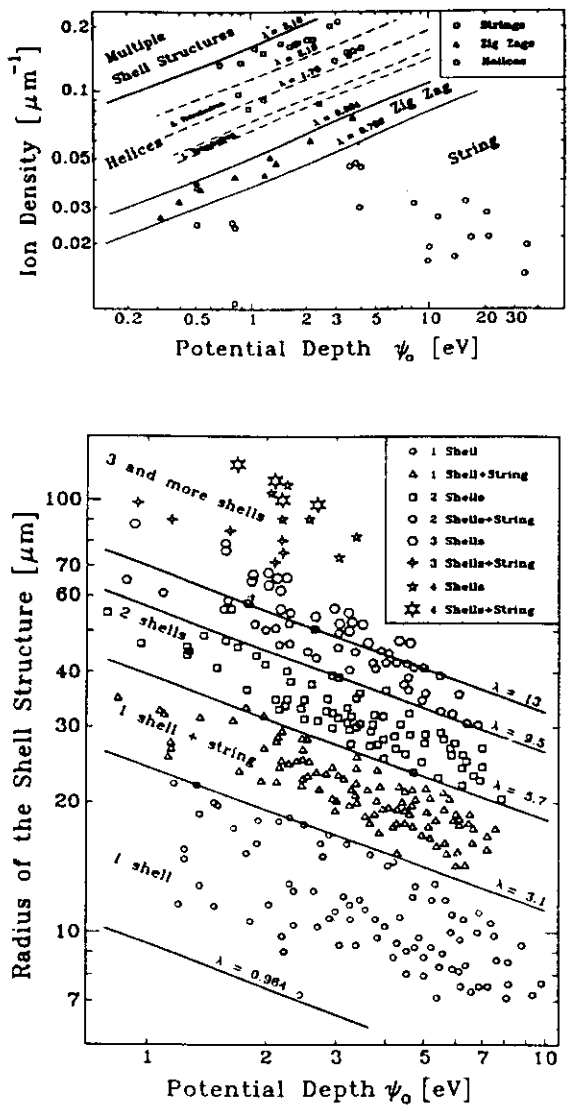

Fig. 10: Summary of the experimental results. Part a: Individual ions resolved, where the observed structures are characterised by the ion density per unit length and the depth of the potential well ψ_o. These two parameters can be combined to give the normalised linear particle density λ which fully determines the ion configuration. The straight lines show critical λ values separating the regions corresponding to the various theoretically expected structures. The observed configurations are labelled with different symbols for each structure. Part b: Individual ions unresolved, where the observed shell structures with up to four shells plus string are characterised by their radius ρ and the potential depth ψ_o. The various observed structures are again separated by lines of theoretically determined critical λ (for details see Ref. 48).

parameters. As the ion density cannot be determined directly from the images, the radius ρ of the structures is used instead as the second parameter. The theoretically predicted boundaries between the different shell structures are again given as straight lines of constant λ following Hasse and Schiffer.[50] The observed ion configurations are

seen once more to be determined by λ for a wide range of potential depths and ion densities.

Our results have important implications for two very different fields. Consider first the physics of low-energy particles: an ion string in a quadrupole ring, being free of micromotion, can be cooled to its vibrational ground state in the confining potential using recently proposed laser cooling techniques.[12] This would place the string in the Lamb-Dicke regime with a vanishing first-order Doppler effect because the spatial amplitude of the motion is smaller than the wavelength of the atomic transition. Furthermore, the second-order Doppler effect, which can only be reduced by further cooling, also disappears making the stored ions very interesting for frequency standards. The large number of ultracold ions available in the ring will lead to a high signal-to-noise ratio. Finally, cooled ions in the ring represent a quantum object of macroscopic dimensions: a Wigner crystal.

With the experimental confirmation that the ordered structures expected in high-energy ion storage rings can indeed be formed, a completely new era of accelerator physics would emerge. The enhanced luminosity of the corresponding beams would allow studies of ionic reactions whose cross sections are too small for investigations in existing accelerators.

A long-term objective for our experiments is to cool an ion crystal to still lower temperatures. Due to the motion driven by the trapping field (micromotion) this is not possible for more than a single ion in a three-dimensional quadrupole trap (Paul trap), as discussed already above. On the other hand, this can be achieved in two-dimensional trapping fields like the quadrupole storage ring or linear ion traps where the free motion in the third dimension is limited by other means. The weak binding of ions in the quadrupole storage ring allows us to apply the wide variety of cooling techniques developed for free atoms. One of the most efficient methods is polarization gradient cooling (PGC).[53–55] In the following, we present the first application of this cooling technique to trapped ions. For details see also Ref. 56).

As the other experiments described here, the laser cooling was performed upon $^{24}Mg^{+}$ ions using the $J_g = 1/2 \rightarrow J_e = 3/2$ transition at a wavelength of 280 nm (natural linewidth $\Gamma = 2\pi \cdot 43MHz$). PGC on this type of transition has been studied extensively in the theoretical literature although the corresponding experimental system has not previously been investigated. The trap of this experiment is the same as the one described above.

However, only a small fraction of the whole storage volume is investigated this time. A weak, electrostatic potential well along the ring circumference with a minimum close to the centre of the observation region enables us to study ensembles of few or even single trapped ions (Fig. 11). This essentially one-dimensional (1D) potential is created by a pair of electrodes separated by about 50 mm, one on either side of the observation region in close proximity to the ring electrodes ($\sim 100\mu m$). Its shape has been mapped by three separate experimental techniques. They are in agreement on the fact that the potential is harmonic with an oscillation frequency ω_z for the ion of $\omega_z = 2\pi \cdot 11.9kHz$ with an error of less than 5 %. The cooling laser field is directed along the ring tangent through the observation region and coincides with

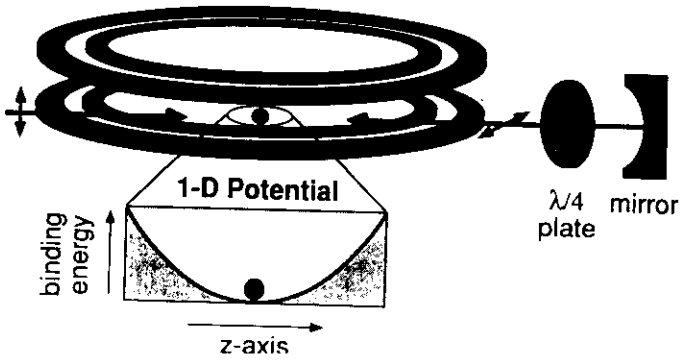

Fig. 11: Experimental schematic with a single ion confined in a quadrupole storage ring. The radial confinement in the secular potential leads to an oscillation frequency of $2\pi \cdot 1MHz$. The ion is only weakly bound along the circumference (see insert). The polarization gradient light field is created by retroreflection of the incoming laser beam with a subsequent double pass through a quarter wave plate. The laser axis is defined as the z-axis.

the z-axis of the 1D potential (Fig. 11). The fluorescence light is detected radially. Despite the curvature of the storage ring, the laser beam deviates less than 5 mrad from the curved minimum of the secular potential over the 500 μm field of view. On the other hand, the coupling of the various degrees of motion in the trapping field is strong enough to cool the radial ion motion to a temperature of several tens of millikelvin for a single trapped ion. Cooling an ensemble of ions reduces the kinetic energy in this component even further due to Coulomb coupling.

Figure 11 displays the scheme for the PGC of the trapped ions. The light field consisting of two counterpropagating orthogonal linearly polarized laser beams (lin $\perp$ lin-configuration). The detuning from the atomic resonance frequency is known to within 2 MHz.

The localization of the ions in a shallow potential well along the laser cooling axis gives us an accurate measure of the temperature. In our experiments, the fluorescence light scattered by the ions is spatially resolved using a photon-counting imaging system. The integration time is five seconds. Consider for the moment a single trapped ion. Determining the spread of the ion's spatial distribution around the equilibrium position allows us to calculate the mean potential energy of the ion. According to the Virial theorem, in a harmonic potential well, this is identical to the mean kinetic energy. Figure 12a shows the position distribution of a single trapped ion in the 1D potential when PGC is applied. As shown, the distribution is well fit by a Gaussian function. Therefore, the kinetic energy of the ion displays the characteristics of a thermal distribution allowing us to assign a temperature T to a specific value of the mean kinetic energy. The following definition has been used. $(1/2)k_BT = \langle E_{kin} \rangle = \langle E_{pot} \rangle = (1/2)M\omega_z^2\langle z^2 \rangle$, where k_B is Boltzmann's constant, M is the ion mass, and $\langle z^2 \rangle$ the variance of the position spread. For the large spatial distribution associated with a shallow potential, this method is quite accurate. However, the addition of more ions to the trap effectively produces a steeper potential due

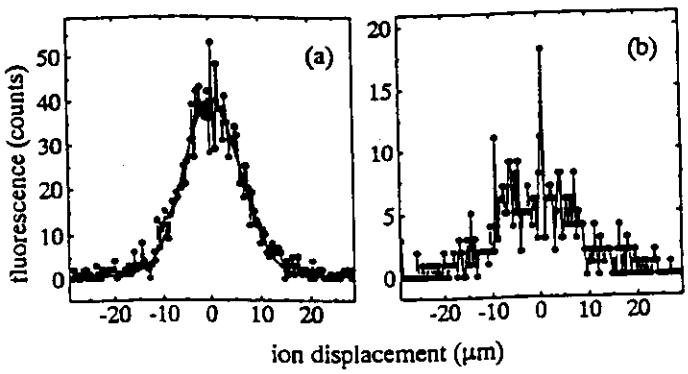

Fig. 12: Measured position distributions for single ions. a) This typical distribution is obtained for $I = 3.3 \cdot 10^{-2} I_{sat}$ and $\delta = -0.5\Gamma$. Its width gives a temperature of $(503 \pm 50)\mu K$. b) A non-Gaussian distribution is found for $I = 3.3 \cdot 10^{-2} I_{sat}$ and $\delta = -1.6\Gamma$. This distribution shows a narrow central structure, however assigning a temperature to such a distribution is not straightforward (see text).

to the mutual Coulomb repulsion and in turn increases the experimental error. For this reason, we focus upon the experiments addressing the cooling of a single trapped ion. In addition, results for a two-ion crystal are presented also.

The minimum observable temperature is defined by the diffraction limit of $0.6\mu m$ of the detection system. Using the known curvature of the potential well, such a diffraction spot leads to a temperature of $1\mu K$. The error in the temperature is due to the finite pixel size of $0.4\mu m$. This error increases with T leading to $\Delta T = 50\mu K$ for a typical $T = 400\mu K$.

Gaussian distributions such as shown in Fig. 12a are found throughout most of the parameter space. However, in the regime where the variance of the ion distribution is minimized, the distributions are not Gaussian. They are characterized by a narrow structure atop a broad Gaussian background (see Fig. 12b). The low kinetic energies associated with these non-Gaussian distributions will be discussed later. For the moment, only the results in the Gaussian regime will be considered.

One of the basic theoretical[57] and experimental[55] results for PGC of neutral atoms is that for large detunings the equilibrium temperature is solely dependent on the amplitude U_o of the light shift, which the atoms experience in a polarization gradient field. The inset of Fig. 13 shows the periodically shifted energies $U_\pm$ of the $m_F = \pm 1/2$ ground states together with U_o. The cooling stems from spontaneous Raman scattering between the two light-shifted ground states. The most probable transition is from the higher-energy ground state to the lower-energy ground state and it reduces the kinetic energy of the atom by an amount close to U_o.

Figure 13 gives a summary of the data presented as a function of $I/\mid\delta\mid$. For large detuning ($\mid\delta\mid \geq \Gamma$) this is proportional to U_o. For small values of $I/\mid\delta\mid$, the two curves follow the same functional dependence. Here, the final temperature is solely defined by $I/\mid\delta\mid$ and so by U_o. As expected, the two curves deviate

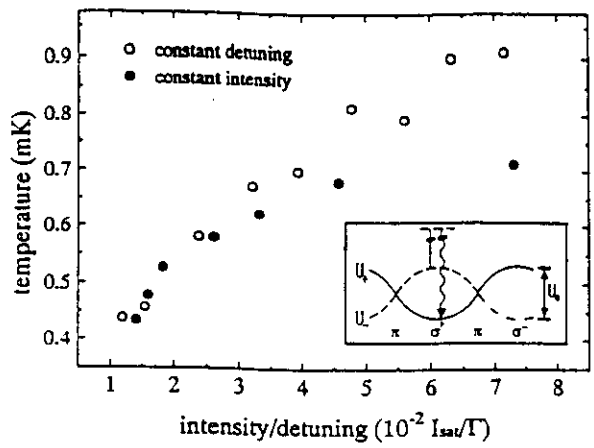

Fig. 13: Ion temperature vs. intensity divided by detuning (o constant detuning, • constant intensity). Qualitatively, the results agree with the predictions of the free-atom theory. On the other hand, the quantitative values leading to the lowest temperatures are two orders of magnitude smaller than for unbound ions. The inset shows the periodic energy shift of the atomic ground states and the fundamental cooling cycle. The miminum temperature we have observed in such a measurement is $T = (300 \pm 50)\mu K$. This is a factor of three below the Doppler limit. This figure is taken from Ref. 56.

for large values of $I/\mid\delta\mid$ since along the constant intensity curve the detuning becomes too small for this simple single-parameter dependence to hold. These results are in qualitative agreement with the free-atom theory. However, the quantitative values of $I/\mid\delta\mid$ leading to the lowest temperatures for the trapped ion are approximately 100 times smaller than for a free atom. In fact, for these smaller values of $I/\mid\delta\mid$, polarization gradient cooling is ineffective for free atoms. We find that for trapped ions the minimum temperature occurs when the depth of the optical potential, U_o, approaches $\hbar\omega_z$. The minimum values displayed in this plot correspond to $U_o = 5\hbar\omega_z$.

This suggests a simple physical picture for the polarization gradient cooling of trapped ions. The trapped ion is truly a quantum-mechanical harmonic oscillator with discrete energy levels. Therefore, the kinetic energy of the ion can best be extracted in units of $\hbar\omega_z$, i.e. the energy quanta of the harmonic oscillator. For that reason, the cooling process is most effective when the energy removed in a PGC cycle, approximately U_o, is equal to a quantum of vibrational energy $\hbar\omega_z$ or a low multiple of this value. Successive spontaneous anti-Stokes Raman-scattering events lead to a ladder of downward transitions through the vibrational states of the harmonic oscillator. In contrast to the free-atom case the final temperature is determined by U_o and ω_z. This reduces to the sole dependence on U_o when ω_z is fixed as in our experiment.

Recent theoretical studies[58–60] of polarization gradient cooling for trapped ions in the weak binding limit ($\omega_z \ll \Gamma$) confirm this physical picture, i.e. the minimum

temperature occurs for $U_o = \hbar\omega_z$. However, this theory makes the additional assumption that the ions are confined to a spatial extent small compared to the wavelength of the cooling transition (Lamb-Dicke limit). The latter condition is not fulfilled in our experiment. This theoretical requirement is not a necessary condition for the functioning of the cooling mechanism, but rather is necessary for the analytical solution of the problem.

For the moment, let us consider one of the more fascinating predictions of the current PGC theories that the minimum kinetic energy attainable is on the order of the energy of the first excited state of the trapping potential. For the case of a weakly bound ion, this can be much lower than the minimum temperature for a free atom. Our observation of non-Gaussian ion distributions supports this prediction. In Fig. 12b, a sharp spike rises at the centre of the trapping potential. This distribution was found for a relatively large detuning and U_o of eleven times $\hbar\omega_z$. The width of this spike is less than 3 picture elements of the imaging system of $1.2\mu m$. If we treat this narrow structure as above, such a localization corresponds to an ion that on average has a temperature of $4\mu K$ and is in the sixth excited state of our 1D trapping potential. Our measurements indicate that the ion maintains this sharp localization for approximately a tenth of our observation time of five seconds. The instability in the localization can be attributed to frequency and intensity fluctuations or perhaps more importantly to the coupling of this 1D motion to the much hotter radial motion. Of course, for such low energies, the single-photon recoil energy plays a significant role in defining the cooling limit. In fact, both the kinetic energy of the ion and the optical trap depth are on the order of the recoil energy. This raises the distinct possibility that the ion is actually trapped in an optical potential well. For our parameters, these wells are quite shallow and at most only the ground state and a single excited state (or band) are bound. The energy of an ion in this first excited state corresponds to a temperature of $7\mu K$. At present, our experimental results are unable to distinguish between these physical descriptions of the sharp localization of the ion. In either case, cooling to a low vibrational state was observed.

We extended the study of PGC of trapped ions to the case of low-density ion crystals (ion strings). Only in a two-dimensional quadrupole trapping field it is possible to cool more than a single ion down to a temperature which is similar to the one obtained for a single ion. For both ions, the position distribution around their mean separation can be fitted by a Gaussian function. In the course of these studies, we found the same quantitative functional dependence of the ion temperature as observed for a single ion. The minimum temperature for a two-ion crystal was found to be $T = (280 \pm 75)\mu K$. This is the coldest 1D ion crystal reported to date. These results clearly show that in a quadrupole storage ring with PGC or other cooling techniques, ensembles of ions can also be cooled far below the Doppler limit.

5. Conclusion

In this paper single ion spectroscopy and the generation of crystalline ion structures in Paul traps have been reviewed. In the last part of the paper experiments

using polarization gradient cooling of ions have been described. In those experiments it was demonstrated that a one-dimensional ion crystal could be cooled far below the Doppler limit.

References

1. W. Neuhauser, M. Hohenstatt, P. Toschek and H. Dehmelt, *Phys. Rev. Lett.* **41** (1978) 233 and *Phys. Rev.* **A22** (1980) 1137.
2. R. H. Dicke, *Phys. Rev.* **89** (1953) 472.
3. D.J. Wineland, W.I. Itano and R.S. Van Dyck, in *Advances in Atomic and Molecular Physics 19*, eds. D. Bates and B. Bederson, p. 136 (Academic Press, Boston 1983).
4. R. Blatt, P. Gill and R.C. Thompson, *Journal of Modern Optics* **39** (1992) 193.
5. R.C. Thompson, in *Advances in Atomic, Molecular and Optical Physics 30*, eds. D. Bates and B. Bederson (Academic Press Inc., Boston 1993), in print.
6. H.G. Dehmelt and F.G. Major, *Phys. Rev. Lett.* **8** (1962) 213.
7. H.A. Schüssler, F.N. Fortson and H. G. Dehmelt, *Phys. Rev.* **187** (1969) 5.
8. W. Paul, O. Osberghaus and E. Fischer, *Forschungsberichte des Wirtschafts- und Verkehrsministeriums Nordrhein-Westfalen*, **415** (1958) 1.
9. E. Fischer, *Z. Phys.* **156**, (1959) 1.
10. D.J. Wineland, W.M. Itano, J.C. Bergquist, J.J. Bollinger and J.D. Prestage, in *Atomic Physics 9*, eds. R.S. van Dyck, Jr. and E.N. Fortson, p. 3 (World Scientific Publishing, Singapore, 1984).
11. H.G. Dehmelt, in *Adv. Atom. Molec. Phys. 3*, eds. D.R. Bates and I. Estermann, p. 53 (Academic, New York, 1967).
12. J. Dalibard, C. Salomon, A. Aspect, E. Arimondo, R. Kaiser, N. Vansteenkiste and C. Cohen-Tannoudji, in *Atomic Physics 11*, eds. S. Haroche, J.C. Gay and G. Grynberg, p. 199 (World Scientific Publishing, Singapore, 1988).
13. F. Diedrich and H. Walther, *Phys. Rev. Lett.* **58** (1987) 203.
14. W. Nagourney, J. Sandberg and H. Dehmelt, *Phys. Rev. Lett.* **56** (1986) 2767.
15. Th. Sauter, W. Neuhauser, R. Blatt and P.E. Toschek, *Phys. Rev. Lett.* **57** (1986) 1696.
16. J.C. Bergquist, R.G. Hulet, W.M. Itano and D.J. Wineland, *Phys. Rev. Lett.* **57** (1986) 1699.
17. U. Eichmann, J.C. Bergquist, J.J. Bollinger, J.M. Gilligan, W.M. Itano, D.J. Wineland and M.G. Raizen, *Phys. Rev. Lett.* **70** (1993) 2359.
18. J.J. Bollinger, D.J. Heinzen, W.M. Itano, S.L. Gilbert and D.J.Wineland, *Phys. Rev. Lett.* **63** (1989) 1031.
19. W.M. Itano, D.J. Heinzen, J.J. Bollinger and D.J. Wineland, *Phys. Rev.* **A41** (1990) 2295.

20. H. Dehmelt, *IEEE Trans. Instrum. Meas.* **31** (1982) 83.

21. J.C. Bergquist, F. Diedrich, W.M. Itano and D.J. Wineland, in *Laser Spectroscopy IX*, eds. M.S. Feld, J.E. Thomas and A. Mooradian (Academic Press, Boston, 1989) p. 274.

22. F. Diedrich, J.C. Bergquist, W.M. Itano and D.J. Wineland, D.J., *Phys. Rev. Lett.* **62** (1989) 403.

23. W. Nagourney, N. Yu and H. Dehmelt, *Opt. Comm.* **79** (1990) 176.

24. J.C. Bergquist, W.M. Itano and D.J. Wineland, *Phys. Rev.* **A36** (1987) 428.

25. H.A. Klein, A.S. Bell, G.P. Barwood and P. Gill, *Appl. Phys.* **B50** (1990) 13.

26. A.S. Bell, P. Gill, H.A. Klein, A.P. Levick, Chr. Tamm and D. Schnier, *Phys. Rev.* **A44** (1991) R20.

27. H. Lehmitz, J. Hattendorf-Ledwoch, R. Blatt and R. Harde, *Phys. Rev. Lett* **62** (1989) 2108.

28. E. Peik, G. Hollemann and H. Walther, *Phys. Rev. A.*, in print.

29. A.A. Madej and J.D. Sankey, *Opt. Lett.* **15** (1990) 634.

30. H. Dehmelt, *Bull. Am. Phys. Soc.* **18** (1973) 1521, ibid. **20** (1975) 60, D. Wineland and H. Dehmelt, *Bull. Am. Phys. Soc.* **20** (1975) 637.

31. M.C. Bigeon, *J. Physique* **28** (1967) 51.

32. R.W. Dunford et al., *Phys. Rev.* **A44** (1991) 764; P. Indelicato et al., *Phys. Rev. Lett.* **68** (1992) 1307, B.B. Birkett et al., *Phys. Rev.* **A47** (1993) R2454.

33. C.A. Schrama, E. Peik, W.W. Smith and H. Walther, *Opt. Comm.* **101** (1993) 32.

34. J.C. Lehmann and C. Cohen-Tannoudji *C. R. Acad. Sc. Paris* **258** (1964) 4463.

35. F. Diedrich, E. Peik, J.M. Chen, W. Quint and H. Walther, *Phys. Rev. Lett.* **59** (1987) 2931.

36. J. Javanainen, *Phys. Rev.* **A33** (1986) 2121; A. Schenzle, R.G. DeVoe and R.G. Brewer, ibid. **33** (1986) 2127; M. Merz, A. Schenzle, *Appl. Phys.* **B50** (1990) 115.

37. J.C. Bergquist, R.G. Hulet, W.M. Itano and D.J. Wineland, *Phys. Rev. Lett.* **57** (1987) 1699.

38. I.I. Sobel'man, in *Atomic Spectra and Radiative Transitions 2* (Springer, Berlin, 1992).

39. P.L. Larkin and P. Hannaford, *Z. Physik D* (in print).

40. F. Diedrich, E. Peik, J.M. Chen, W. Quint and H. Walther, *Phys. Rev. Lett.* **59** (1987) 2931.

41. R. Blümel, J.M. Chen, F. Diedrich, E. Peik, W. Quint, W. Schleich, Y.R. Shen and H. Walther, in *Atomic Physics 11*, eds. S. Haroche, J.C. Gay and G. Grynberg, p. 243 (World Scientific Publishing, Singapore, 1988).

42. R. Blümel, J.M. Chen, W. Quint, W. Schleich, Y.R. Shen and H. Walther, *Nature* **334** (1988) 309.

43. R. Blümel, C. Kappler, W. Quint and H. Walther, *Phys. Rev.* **A40** (1989) 808.

44. J. Drees and W. Paul, *Z. Phys.* **180** (1964) 340.

45. D.A. Church, *J. Appl. Phys.* **40** (1969) 3127.

46. H. Walther, in *Proc. of the Workshop on Light Induced Kinetic Effects on Atoms, Ions and Molecules*, eds. L. Moi, S. Gozzini, C. Gabbanini, E. Arimondo and F. Strumia) (ETS Editrice, Pisa, 1991).

47. I. Waki, S. Kassner, G. Birkl and H. Walther, *Phys. Rev. Lett.* **68** (1992) 2007.

48. G. Birkl, S. Kassner and H. Walther, *Nature* **357** (1992) 310.

49. A. Rahman and J.P. Schiffer, Phys. Rev. Lett. **57** (1986) 1133.

50. R.W. Hasse and J.P. Schiffer, *Ann. Phys.* **203** (1990) 419.

51. M.G. Raizen, J.M. Gilligan, J.C. Berquist, W.M. Itano, and D.J. Wineland, *Journ. Mod. Opt.* **39** (1992) 233.

52. S.L. Gilbert, J.J. Bollinger and D.J. Wineland, *Phys. Rev. Lett.* **60** (1988) 2022.

53. J. Dalibard and C. Cohen-Tannoudji, *J. Opt. Soc. Am. B* **6** 2023 (1989).

54. P.D. Lett, R.N. Watts, C.I. Westbrook, W.D. Philips, P.L. Gould and H.J. Metcalf, *Phys. Rev. Lett.* **61** (1988) 169.

55. C. Salomon, J. Dalibard, W.D. Philips, A. Clairon and S. Guellati, *Europhys. Lett.* **12** (1990) 683.

56. G. Birkl, J.A. Yeazell, R. Rückerl, H. Walther, *Europhys. Lett.* **27** (1994) 197.

57. Y. Castin and J. Dalibard, *Europhys. Lett.* **14** (1991) 761.

58. Yoo Sung Mi and J. Javanainen, *Phys. Rev. A* **48** (1993) R30; J. Javanainen and Yoo Sung Mi, *Phys. Rev. A* **48** (1993) 3776.

59. J.I. Cirac, R. Blatt, A.S. Parkins and P. Zoller, *Phys. Rev. A* **48** (1993) 1434.

60. Li Yongqing and K. Mølmer, *Laser Physics* **4** (1994) 829.

Resonance Fluorescence of a Single Ion*

J. T. Höffges, H.W. Baldauf, T. Eichler, S.R. Helmfrid and H. Walther

Max-Planck-Institut für Quantenoptik and
Sektion Physik der Universität München
85748 Garching, Fed. Rep. of Germany

Abstract:

The spectrum of the fluorescent radiation of a single trapped $^{24}Mg^{+}$-ion at low excitation intensity was investigated. The measurement was performed by heterodyning the fluorescent radiation with a sideband of the single mode laser radiation used to excite the ion, resulting in a linewidth of 6 Hz. Under identical experimental conditions, the antibunching in the photon statistics of the fluorescent radiation was also investigated. Heterodyne detection and photon correlation measurement are complementary featuring either the wave or the particle nature of the radiation.

Introduction

Resonance fluorescence of atoms is a basic process in radiation-atom interactions, and has therefore always generated considerable interest. The methods of experimental investigation have changed continuously due to the availability of new experimental tools. A considerable step forward occurred when tunable and narrow band dye laser radiation became available. These laser sources are sufficiently intense to easily saturate an atomic transition. In addition, the lasers provide highly monochromatic light with coherence times much longer than typical natural lifetimes of excited atomic states. Excitation spectra with laser light using well collimated atomic beam lead to a width being practically the natural width of the resonance transition, therefore it became possible to investigate the frequency spectrum of the fluorescence radiation with high resolution. However, the spectrograph used to analyze the reemitted radiation was a Fabry-Perot interferometer, the resolution of which did reach the natural width of the atoms, but was insufficient to reach the laser linewidth, see e.g. [1, 2]. A considerable progress in this direction was achieved by investigating the fluorescence spectrum of ultra-cold atoms in an optical lattice in a heterodyne experiment (Jessen et al. [3]). In these measurements a linewidth of 1 kHz was achieved, however, the quantum aspects of the resonance

*This paper is dedicated to Professor Ingvar Lindgren on the occasion of his 65th birthday

fluorescence such as antibunched photon statistics cannot be investigated under these conditions since they wash out when more than one atom is involved.

Thus the ideal experiment requires a single atom to be investigated. Since some time it is known that ion traps allow to study the fluorescence from a single laser cooled particle practically at rest, thus providing the ideal case for the spectroscopic investigation of the resonance fluorescence. The other essential ingredient for achievement of high resolution is the measurement of the frequency spectrum by heterodyning the scattered radiation with laser light as demonstrated with many cold atoms. Such an optimal experiment with a single trapped Mg^+ ion is described in this paper. The measurement of the spectrum of the fluorescent radiation at low excitation intensities is presented. Furthermore, the photon correlation of the fluorescent light has been investigated under practically identical excitation conditions. The comparison of the two results shows a very interesting aspect of complementarity since the heterodyne measurement corresponds to a "wave" detection of the radiation whereas the measurement of the photon correlation is a "particle" detection scheme. It will be shown that under the same excitation conditions the wave detection provides the properties of a classical atom, i.e. a driven oscillator, whereas the particle or photon detection displays the quantum properties of the atom. Whether the atom displays classical or quantum properties thus depends on the method of observation.

The spectrum of the fluorescence radiation is given by the Fourier transform of the first order correlation function of the field operators, whereas the photon statistics and photon correlation is obtained from the second order correlation function. The corresponding operators do not commute, thus the respective observations are complementary. Present theory on the spectra of fluorescent radiation following monochromatic laser excitation can be summarized as follows: fluorescence radiation obtained with low incident intensity is also monochromatic owing to energy conservation. In this case, elastic scattering dominates the spectrum and thus one should measure a monochromatic line at the same frequency as the driving laser field. The atom stays in the ground state most of the time and absorption and emission must be considered as one process with the atom in principle behaving as a classical oscillator. This case was treated on the basis of a quantized field many years ago by Heitler [4]. With increasing intensity upper and lower states become more strongly coupled leading to an inelastic component, which increases with the square of the intensity. At low intensities, the elastic part dominates since it depends linearly on the intensity. As the intensity of the exciting light increases, the atom spends more time in the upper state and the effect of the vacuum fluctuations comes into play through spontaneous emission. The inelastic component is added to the spectrum, and the elastic component goes through a maximum where the Rabi flopping frequency $\Omega = \Gamma/\sqrt{2}$ (Γ is the natural linewidth) and then disappears with growing Ω. The inelastic part of the spectrum gradually broadens as Ω

increases and for $\Omega > \Gamma/2$ sidebands begin to appear. For a saturated atom, the form of the spectrum shows three well-separated Lorentzian peaks. The central peak has width Γ and the sidebands which are each displaced from the central peak by the Rabi frequency are broadened to $3\Gamma/2$. The ratio of the height of the central peak to the sidebands is 3:1. This spectrum was first calculated by Mollow [5]. For other relevant papers see the review of Cresser et al. [2].

Experimental Setup and Results

The experimental study of the problem requires, as mentioned above, a Doppler-free observation. In order to measure the frequency distribution, the fluorescent light has to be investigated by means of a high resolution spectrometer. The first experiments of this type were performed by Schuda et al. [6] and later by Walther et al. [7], Hartig et al. [7, 1] and Ezekiel et al. [8]. In all these experiments, the excitation was performed by single-mode dye laser radiation, with the scattered radiation from a well collimated atomic beam observed and analyzed by Fabry-Perot interferometers. Experiments to investigate the elastic part of the resonance fluorescence giving a resolution better than the natural linewidth have been performed by Gibbs et al. [9] and Cresser et al [2].

The first experiments which investigated antibunching in resonance fluorescence were also performed by means of laser-excited collimated atomic beams. The initial results obtained by Kimble, Dagenais, and Mandel [10] showed that the second-order correlation function $g^{(2)}(t)$ had a positive slope which is characteristic of photon antibunching. However, $g^{(2)}(0)$ was larger than $g^{(2)}(t)$ for $t \rightarrow \infty$ due to number fluctuations in the atomic beam and to the finite interaction time of the atoms [11, 12]. Further refinement of the analysis of the experiment was provided by Dagenais and Mandel [11]. Rateike et al. [13] used a longer interaction time for an experiment in which they measured the photon correlation at very low laser intensities (see Ref. [2] for a review). Later, photon antibunching was measured using a single trapped ion in an experiment which avoids the disadvantages of atom number statistics and finite interaction time between atom and laser field [14].

As pointed out in many papers photon antibunching is a purely quantum phenomenon (see e.g. Refs. [2, 15]. The fluorescence of a single ion displays the additional nonclassical property that the variance of the photon number is smaller than its mean value (i.e. it is sub-Poissonian). This is because the single ion can emit only a single photon and has to be re-excited before it can emit the next one which leads to photon emissions at almost equal time intervals. The sub-Poissonian statistics of the fluorescence of a single ion has been measured in a previous experiment [14] (see also Ref. [16] for comparison).

The trap used for the present experiment was a modified Paul-trap, called an end-cap-trap [17] (see Fig. 1) which produces good confinement of the trapped ion. Therefore, the number of sidebands in the fluorescence spectrum, caused by the oscillatory motion of the laser cooled ion in the pseudopotential of the trap, is reduced. The trap consists of two solid copper-beryllium cylinders (diameter 0.5 mm) arranged co-linearly with a separation of 0.56 mm. These correspond to the cap electrodes of a traditional Paul trap, whereas the ring electrode is replaced by two hollow cylinders, one of which is concentric with each of the cylindrical endcaps. Their inner and outer diameters are 1 and 2 mm ,respectively and they are electrically isolated from the cap electrodes. The fractional anharmonicity of this trap configuration, determined by the deviation of the real potential from the ideal quadrupole field is below 0.1 % [17]. The trap is driven at a frequency of 24 MHz with typical secular frequencies in the xy-plane of approximately 4 MHz. This required a radio-frequency voltage with an amplitude on the order of 300 V to be applied between the cylinders and the endcaps, and with AC-grounding of the outer electrodes provided through a capacitor.

The measurements were performed using the $3^2S_{1/2}$ - $3^2P_{3/2}$ transition of the $^{24}Mg^+$-ion at a wavelength of 280 nm. The natural width of this transition is 42.7 MHz. The exciting laser light was produced by frequency doubling the light from a rhodamine 110 dye laser. The laser was tuned slightly below resonance in order to Doppler-cool the secular motion of the ion. All the measurements of the fluorescent radiation described in this paper were performed with this slight detuning.

For the experiment described here, it is important to have the trapped ion at rest as far as possible to minimize the light lost into motional sidebands. There are two reasons which may cause motion of the ion: the first one is the periodic oscillation of the ion within the harmonic pseudopotential of the trap and the second one is micromotion which is present when the ion is not positioned exactly at the saddle point of the trap potential. Such a displacement may be caused by a contact potential resulting, for example, by a coating of the electrodes by Mg produced when the atoms are evaporated during the loading procedure of the trap. Reduction of the residual micromotion can be achieved by adjusting the position of the ion with DC-electric fields generated by additional electrodes. For the present experiment they were arranged at an angle of 120° in a plane perpendicular to the symmetry axis of the trap electrodes. By applying auxiliary voltages (U_1 and U_2) to these electrodes and U_U and U_D to the outer trap electrodes (Fig. 1), the ion's position can be adjusted to settle at the saddle point of the trap potential.

← Fig 1

The micromotion of the ion can be monitored using the periodic Doppler shift at the driving frequency of the trap which results in a periodic intensity modulation in the fluorescence intensity. This modulation can be measured by means of a tran-

sient recorder, triggered by the AC-voltage applied to the trap. There are three laser beams (lasers 1-3 in Fig. 2) passing through the trap in three different spatial directions which allow measurement of the three components of the micromotion separately. By adjusting the compensation voltages U_1, U_2, U_U and U_D the amplitude of the micromotion could be reduced to a value smaller than $\lambda/8$ in all spatial directions.

The amount of secular motion of the ion resulting from its finite kinetic energy cannot be tested by this method since the secular motion is not phase coupled to the trap voltage. However, the intensity modulation owing to this motion can be seen in a periodic modulation of the photon correlation signal. For all measurements presented here, this amplitude was below $\lambda/5$. This correspnds to the ion having a temperature of approximately 1 mK and a mean vibrational occupation of n=5, which results in less than 50 % of the fluorescence energy being lost into the vibrational sidebands.

The heterodyne measurement is performed as follows. The dye laser excites the trapped ion with frequency ω_L while the fluorescence is observed in a direction of about 54° to the exciting laser beam (see Fig. 2). However, both the observation direction and the laser beam are in a plane perpendicular to the symmetry axis of the trap. Before reaching the ion, a fraction of this laser radiation is removed with a beamsplitter and then frequency shifted (by 137 MHz with an acousto-optic modulator (AOM)) to serve as the local oscillator. The local oscillator and fluorescence radiations are then overlapped and simultaneously focused onto the photodiode where the initial frequency mixing occurs. The frequency difference signal is amplified by a narrow band amplifier and then frequency down-converted to 1 kHz so that it could be analyzed by means of a fast Fourier analyzer (FFT). The intermediate frequency for this mixing of the signal was derived from the same frequency-stable synthesizer which was used to drive the accousto-optic modulator producing the sideband of the laser radiation so that any synthesizer fluctuations are canceled out.

← Fig 2

An example of a heterodyne signal is displayed in Fig. 3, where $\Delta\omega$ is the frequency difference between the heterodyne signal and the driving frequency of the AOM. Frequency fluctuations of the laser beam cancel out and do not influence the linewidth because at low intensity the fluorescence radiation always follows the frequency of the exciting laser while the local oscillator is derived directly from the same laser beam. The residual linewidth results mainly from fluctuations in the optical path length of the local oscillator or of the fluorescent beam. Both beams pass through regular air and it was observed that a forced motion of the air increased the frequency width of the heterodyne signal. The frequency resolution of the FTT was 3.75 Hz for the particular measurement. The heterodyne measure-

ments were performed at a saturation parameter $s = \frac{\Omega^2/2}{\Delta^2 + (\Gamma^2/4)}$ of 0.9, where Δ is the laser detuning. In this region, the elastic part of the fluorescent spectrum has a maximum [18].

← Fig 3

The signal to noise ratio observed in the experiment is shot noise limited. The signal in Fig. 3 corresponds to a rate of the scattered photons of about 10^4 s^{-1} which is an upper limit since photons were lost from detection due to scattering into sidebands caused by the secular motion of the ion. In order to reduce this loss as much as possible, a small angle between the directions of observation and excitation was used.

Investigation of photon correlations employed the ordinary Hanbury-Brown and Twiss setup with two photomultipliers and a beam splitter. The setup was essentially the same as described in Ref. [14]. The pulses from the photomultipliers (RCA C31034-A02) were amplified and discriminated by a constant fraction discriminator (EG&G model 584). The time delay t between the photomultiplier signals was converted by a time-to-amplitude converter into a voltage amplitude proportional to the time delay. A delay line of 100 ns in the stop channel allowed for the measurement of $g^{(2)}(t)$ for both positive and negative t in order to check the symmetry of the measured signal. The output of the time-to-amplitude converter was accumulated by a multichannel analyzer in pulse height analyzing mode. Three typical measurements, each at small values of s but with different detunings, are shown in Fig. 4. The detunings and Rabi frequencies were determined by fitting the formula given in Ref. [12] to the measurements. For small time delays (< 20 ns) the nonclassical antibunching effect is observed, superposed with Rabi oscillations which are damped out with a time constant corresponding to the lifetime of the excited state.

← Fig 4

A measurement of $g^{(2)}(t)$ with an averaging time of hours and time delays up to 500 ns resulted in no visible micromotion effects when the compensation voltages U_1, U_2, U_U and U_D were correctly adjusted. Micromotion results in a periodic modulation of the photon correlation at the driving frequency of the trap (compare Ref. [14]). The stray-light counting rate was so low that there was no need to correct the measurement shown in Fig. 4 (b) for accidental counts. There was actually not a single count in the t = 0 channel within the integration time of 220 min.

Conclusions

In conclusion, we have presented the first high-resolution heterodyne measurement of the elastic peak in resonance fluorescence of a single ion. At identical experimental parameters we have also measured antibunching in the photon correlation

of the scattered field. Together, both measurements show that, in the limit of weak excitation, the fluorescence light differs from the excitation radiation in the second-order correlation but not in the first order correlation. However, the elastic component of resonance fluorescence combines an extremely narrow frequency spectrum with antibunched photon statistics, which means that the fluorescence radiation is not second-order coherent as expected from a classical point of view. This apparent contradiction can be explained easily by taking into account the quantum nature of light, since first-order coherence does not imply second-order coherence for quantized fields [19]. The heterodyne and the photon correlation measurement are complementary since they emphasize either the classical wave properties or the quantum properties of resonance fluorescence, respectively.

In a recent treatment of a quantized trapped particle [20] it was shown that a trapped ion in the vibrational ground state of the trap will also show the influence of the micromotion since the wavefunction distribution of the ion is pulsating at the trap frequency. This means that a trapped particle completely at rest will also scatter light into the micromotion sidebands. Investigation of the heterodyne spectrum at the sidebands may give the chance to confirm these findings. It is clear that such an experiment will not be easy since other methods are needed to verify that the ion is actually at rest at the saddle point of the potential .

Acknowledgements

We would like to thank Roy Glauber for many discussions in connection with his quantum treatment of a trapped particle. We also thank Girish S. Agarwal for many discussions.

References

[1] Hartig, W., Rasmussen, W. Schieder, R., Walther, H. (1976). *Z. Physik* **A278**, 205.

[2] Cresser, J. D., Häger, J., Leuchs, G., Rateike, F. M., Walther, H. (1982). *Topics in Current Physics* **27**, 21.

[3] Jessen, P.S., Gerz, C., Lett, P.D., Philipps, W.D., Rolston, S.L., Spreuuw, R.J.C., and Westbrook, C.I. (1992). *Phys. Rev. Lett.* **69**, 49.

[4] Heitler, W. (1954). *The Quantum Theory of Radiation*, Third Edition, p. 186, Oxford University Press.

[5] Mollow, B.R. (1969). *Phys. Rev.* **188**, 1969.

[6] Schuda, F., Stroud, C., Jr., Hercher, M. (1974). *J. Phys.* **B1**, L198.

[7] Walther, H. (1975). *Lecture Notes in Physics* **43**, Springer, p. 358.

[8] Wu, F. Y., Grove, R. E., Ezekiel, S. (1975). *Phys. Rev. Lett.* **35**, 1426; Grove, R.E., Wu, F. Y., Ezekiel, S. (1977). *Phys. Rev. Lett.* **A 15**, 227.

[9] Gibbs H.M. and Venkatesan, T.N.C. (1976). *Opt. Comm.* **17**, 87.

[10] Kimble, H. J., Dagenais, M., and Mandel, L. (1977). *Phys. Rev. Lett.* **39**, 691.

[11] Jakeman, E., Pike, E. R., Pusey, P. N., and Vaugham, J. M. (1977). *J. Phys.* **A 10**, L257.

[12] Kimble, H. J., Dagenais, M., and Mandel, L. (1978). *Phys. Rev.* **A 18**, 201; Dagenais, M., Mandel, L. (1978). *Phys. Rev.* **A 18**, 2217.

[13] Rateike, F.-M., Leuchs, G., and Walther, H., results cited in Ref. [2].

[14] Diedrich, F., Walther, H. (1987). *Phys. Rev. Lett.* **58**, 203.

[15] Walls, D.F. (1979). *Nature* **280**, 451.

[16] Short, R. and Mandel, L. (1983). *Phys. Rev. Lett.* **51**, 384, and in *Coherence and Quantum Optics V*, p. 671 (L. Mandel and E. Wolf, eds.), Plenum, New York, 1984.

[17] Schrama, C. A., Peik, E., Smith, W. W., and Walther, H. (1993). *Opt. Comm.* **101**, 32.

[18] Cohen-Tannoudji, C., Dupont-Roc, J., Grynberg, G. (1992). *Atom-Photon Interactions*, J. Wiley & Sons, Inc.

[19] Loudon, R. (1980). *Rep. Progr. Phys.* **43**, 913.

[20] Glauber, R. (1992). *Proceedings of the International School of Physics "Enrico Fermi", Course CXVIII Laser Manipulation of Atoms and Ions*, p. 643 (E. Arimondo, W.D. Phillips, F. Strumia, eds.), North Holland.

Figure Captions

Fig. 1: Electrode configuration of the endcap trap. The open structure offers a large detection solid angle and good access for laser beams testing the micromotion of the ion. Micromotion is minimized by applying dc voltages: U_1, U_2, U_U, U_D.

Fig. 2: Scheme of heterodyne detection. The trap is omitted in the figure with only two of the compensation electrodes shown. Laser 3 is directed at an angle of 22° with respect to the drawing plane and Laser 2.

Fig. 3: Heterodyne spectrum of a single trapped $^{24}Mg^+$-ion for $s = 0.9$, $\Delta = -2.3\ \Gamma$, $\Omega = 3.2\ \Gamma$. Integration time: 267 ms.

Fig. 4: Antibunching signals of a single $^{24}Mg^+$-ion. The integration time t_0 was limited by the storage time of the ion. (a), $\Delta = -2.3\ \Gamma$, $\Omega = 2.8\ \Gamma$. $s = 0.7$ and $t_0 =$ 165 min. (b) $\Delta = -1.1\ \Gamma$, $\Omega = 1.0\ \Gamma$. $s = 0.3$ and $t_0 = 95$ min. (c) $\Delta = -0.5\ \Gamma$, $\Omega =$ $0.6\ \Gamma$. $s = 0.4$ and $t_0 = 220$ min. The solid line is a theoretical fit, see text for details.

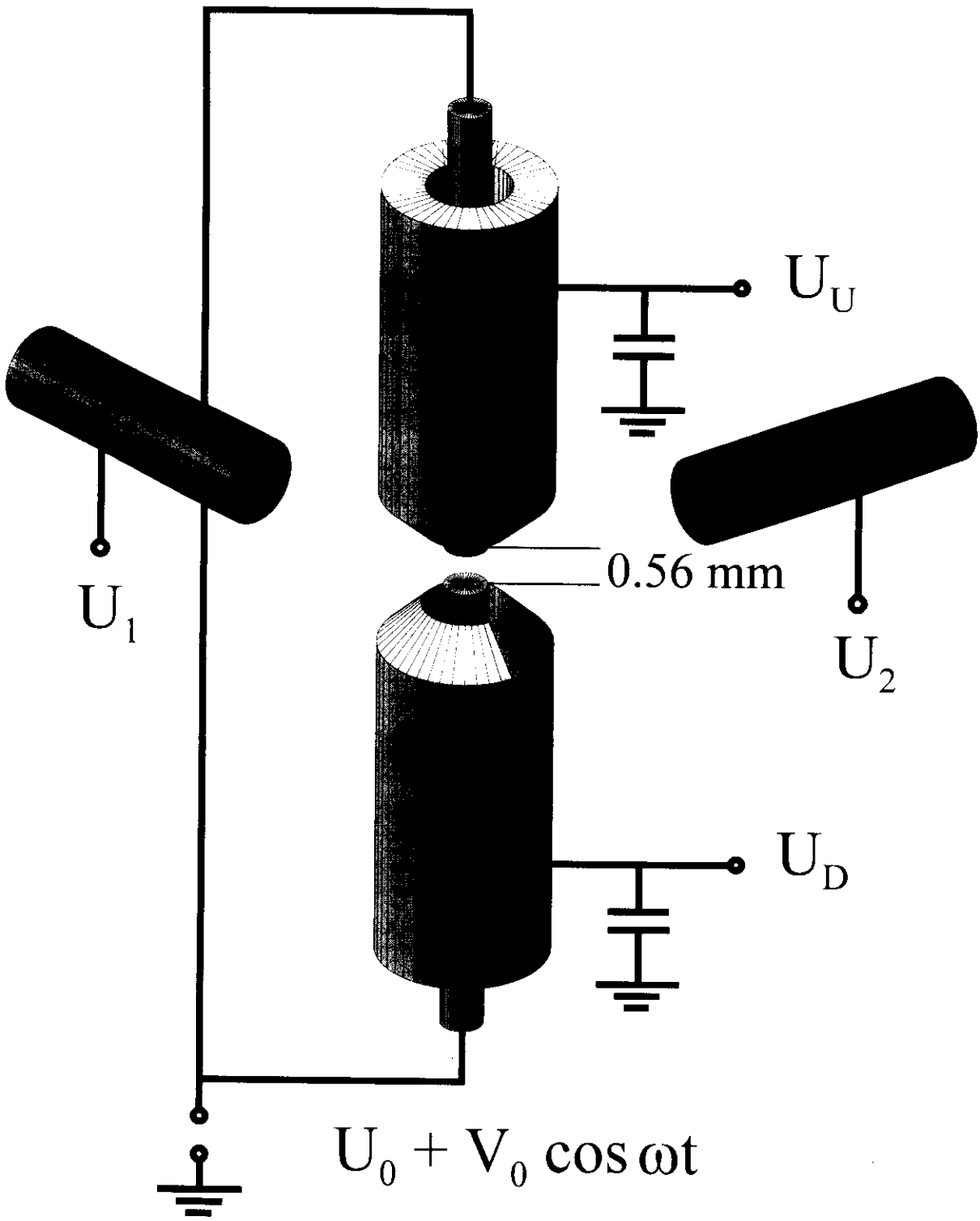

Fig. 1

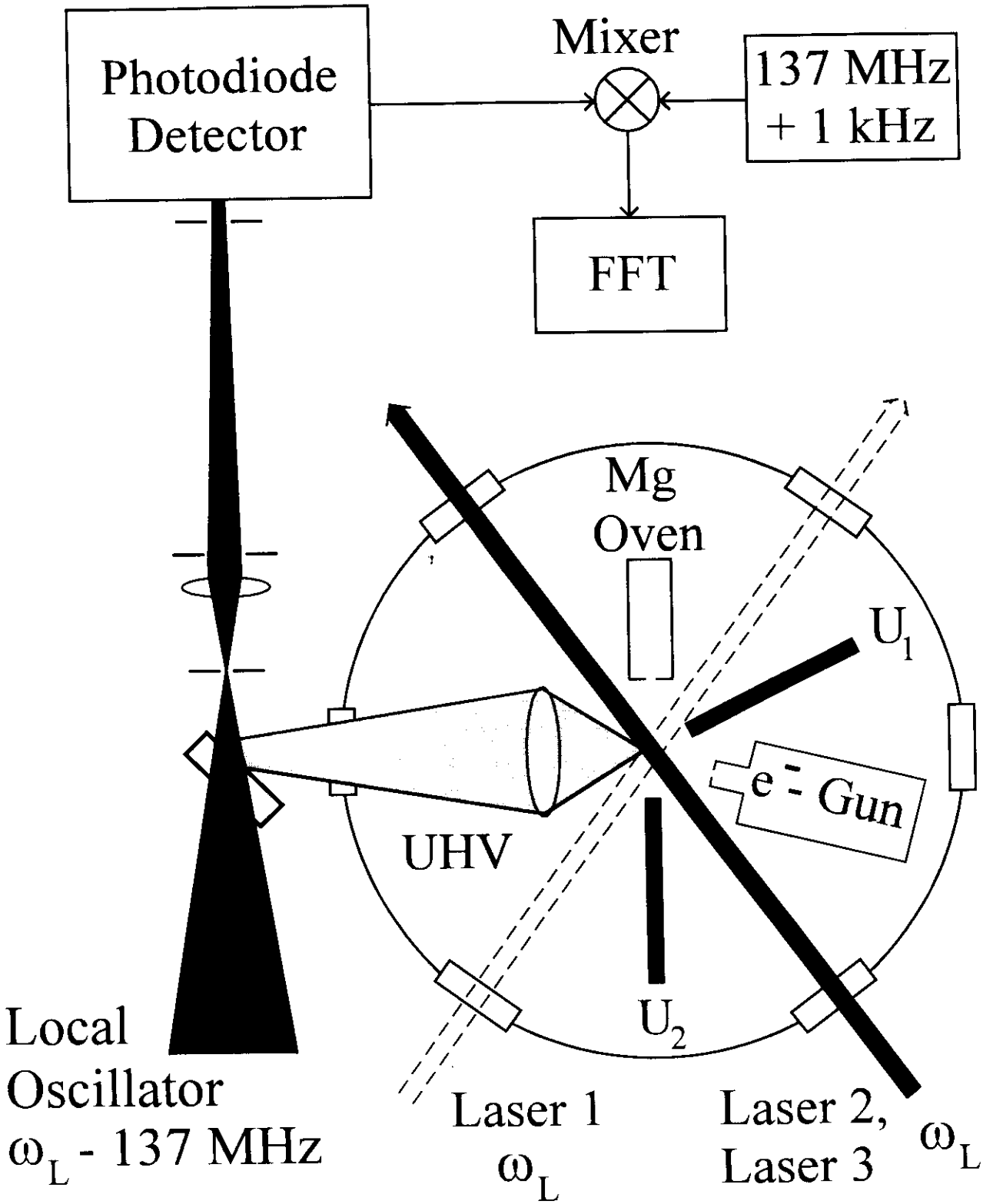
Photodiode Detector
Mixer
137 MHz + 1 kHz
FFT
Mg Oven
U_1
e⁻ Gun
UHV
U_2
Local Oscillator
ω_L - 137 MHz
Laser 1
ω_L
Laser 2, Laser 3
ω_L

Fig. 2

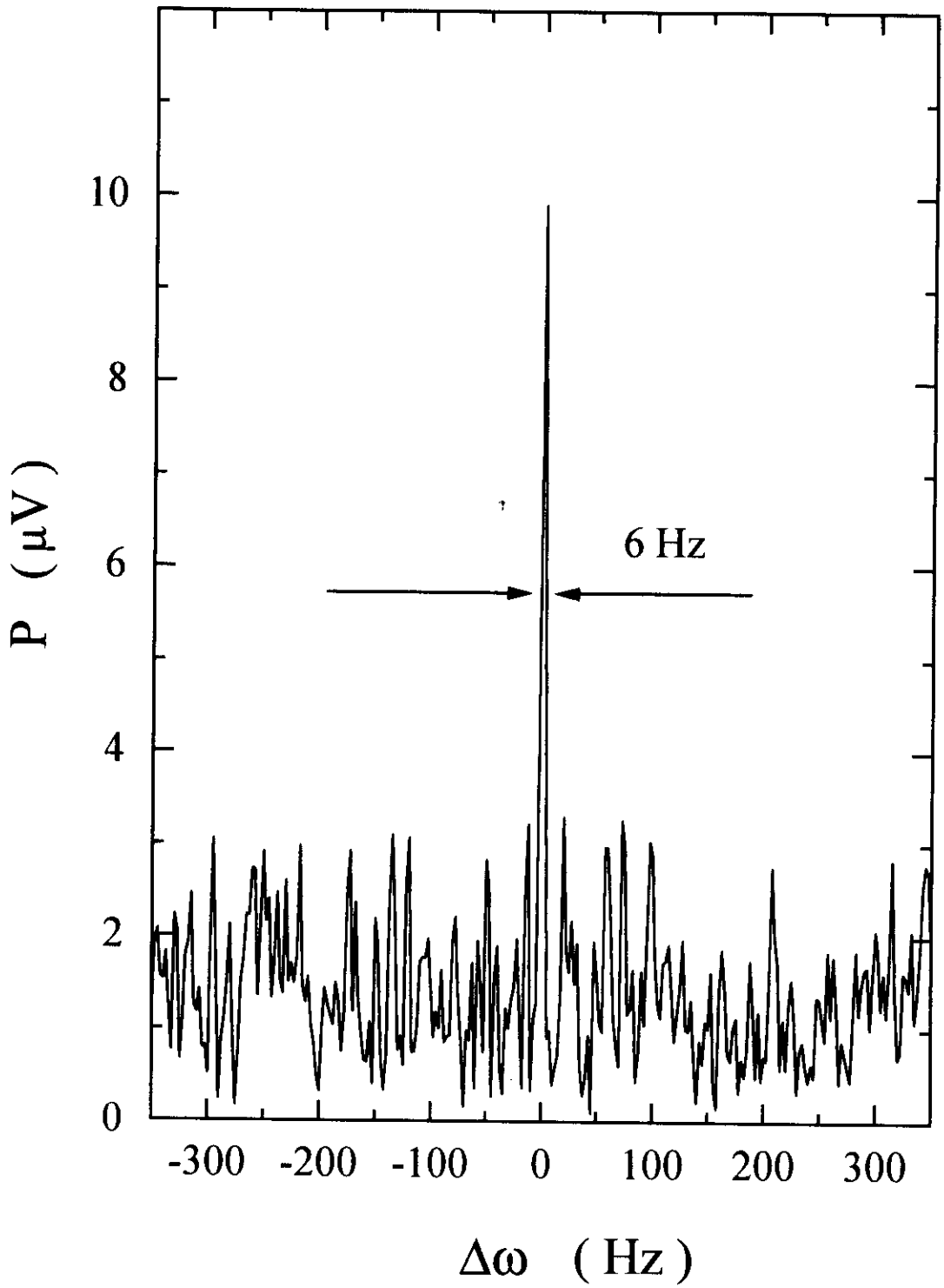

Fig. 3

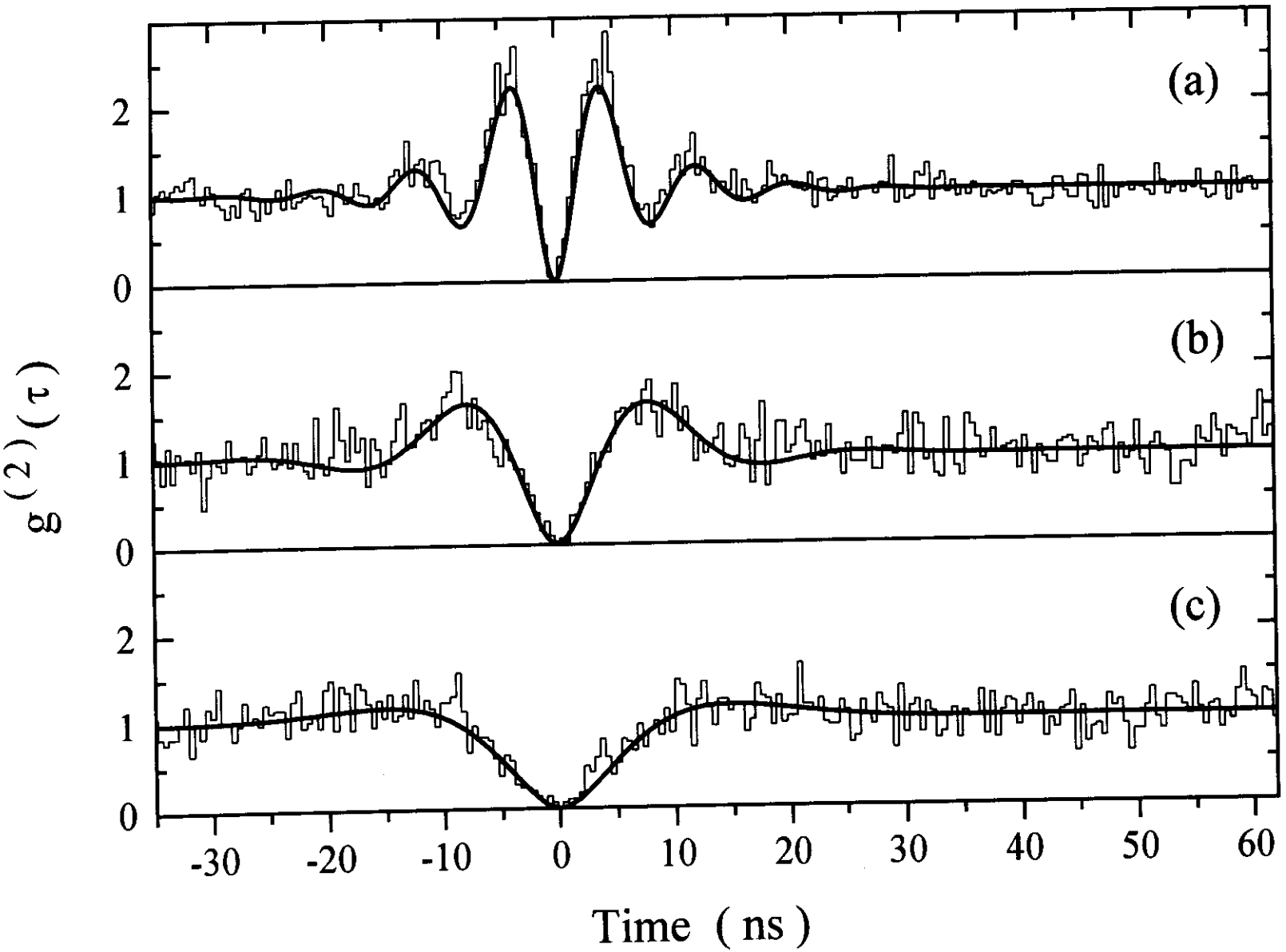

Fig. 4